ADVANCED THERMAL MANAGEMENT OF HIGH TEMPERATURE FUEL CELLS VIA ACTIVE FLOW CONTROL

A Thesis
Presented to
The Academic Faculty

by

Patrick Louka

In Partial Fulfillment
of the Requirements for the Degree
Masters of Science in the
School of Mechanical Engineering

Georgia Institute of Technology
May, 2007

ADVANCED THERMAL MANAGEMENT OF HIGH TEMPERATURE FUEL CELLS VIA ACTIVE FLOW CONTROL

Approved by:

Dr. Comas L. Haynes, Co-Advisor
Aerospace, Transportation, and Advanced Systems Laboratory
Georgia Tech Research Institute

Dr. William J. Wepfer
School of Mechanical Engineering
Georgia Institute of Technology

Dr. David E. Parekh
School of Mechanical Engineering
Georgia Institute of Technology

Date Approved: April 4, 2007

ACKNOWLEDGEMENTS

I wish to thank Dr. Comas Haynes for his continued involvement and guidance in my research and professional growth. Without his help, this project would have never been started. I would like to thank Robert Englar for his expertise with the Coanda effect and allowing the use of the model test facilities. I greatly appreciate the help of Malik Little in his assistance throughout the project with testing, locating materials, developing contacts, and brainstorming ideas. Warren Lee has been a great resource in helping to troubleshoot many of the data acquisition issues encountered. I would like to thank Dr. William Wepfer and Dr. David Parekh for providing me with guidance as my thesis committee members. I would also like to thank Dr. Wayne Whiteman for helping me secure funding and valuable experience so that I could conduct this research effort. I appreciate the learning environment and sound knowledge the Woodruff School of Mechanical Engineering has provided me. I would like to thank GTRI and the FACES research scholarship for providing initial funding to get this research effort started. Jimmy Ross was extremely helpful in providing me services in the machine shop at a reduced cost. I would like to thank my parents for providing me with the motivation and support that has brought me to this point. I would like to thank Sarah Kittridge, who has shown loving support through my stay at Georgia Tech.

TABLE OF CONTENTS

LIST OF TABLES

Page

LIST OF FIGURES

LIST OF SYMBOLS

h^*	Methalpy – Enthalpy, Potential Energy, and Kinetic Energy
ρ	Density
q	Heat addition into the control volume
t	time
P	Pressure
Φ	Local volumetric heating due to viscous dissipation
μ	Dynamic Viscosity
$\frac{du}{dy}$	Velocity gradient in the radial direction
S_x	Sample standard deviation
U_R	Statistical uncertainty in the recirculation ratio
R	Recirculation ratio

$$R = \frac{\dot{m}_{air,circulated}}{\dot{m}_{air,externally\,supplied}}$$

$\dot{m}_{\text{air,circulated}}$	Mass flow rate of air circulating through the stack
$\dot{m}_{\text{air,externally supplied}}$	Mass flow rate of air externally supplied to the tunnel
P_{dyn}	Dynamic pressure downstream of the stack
P_{stat}	Static Pressure downstream of the stack
v	Velocity of air through the stack
R_{air}	Gas constant for air
$T_{air,DS}$	Temperature of the air leaving the stack
A	Cross-sectional area where the total pressure is read
P_{inlet}	Inlet Pressure to the critical flow nozzle

T_{amb} Ambient temperature at the flow nozzle

T^* Thermal mixing ratio used to describe the degree of thermal mixing

$$T^* = \frac{T_{air,upstream} - T_{air,inlet}}{T_{stack} - T_{air,inlet}}$$

$T_{air,upstream}$ Air temperature upstream of the stack location

$T_{air,inlet}$ Air temperature coming out of the plenum

T_{stack} Temperature of the stack

$\sum_{in} \dot{m}_i$ Sum of the mass flow into the control volume

$\sum_{out} \dot{m}_j$ Sum of the mass flow out of the system

$\dot{Q}_{in}$ Input heat rate into the control volume

$\dot{W}_{in}$ Power input into the control volume

$\dot{Q}_{out}$ Input heat rate into the control volume

$\dot{W}_{out}$ Power input into the control volume

h Enthalpy

$\dot{I}$ Exergy destruction

C_p Heat Capacity

$I_{equivalent}$ Equivalent (Stoichiometric) current from the stack

$NOS_{supplied}$ Multiple of molar oxygen supplied to the stack over stoichiometric electrochemistry (actual to theoretical oxidant supply)

β Moles of air per mole of O_2

M_{air} Molar mass of air

n Number of electrons per mol of O_2

F Faraday's constant (96485.3415 coulombs)

V_{cell} Voltage of a single cell

q_{rxn}	Heat release from the electrochemical reaction

LIST OF ABBREVIATIONS

SOFC	Solid Oxide Fuel Cell
PEMFC	Proton Exchange Membrane Fuel Cell
YSZ	Yttria (Y_2O_3) Stabilized Zirconia (ZrO_2)
SMR	Steam Methane Reformer
RRFCS	Rolls Royce Fuel Cell Systems
MSP	Multiple Supply Point
CFN	Critical Flow Nozzle
EA	Exit Area
US	Upstream
DS	Downstream
ESP pressure scanners	Electronic Silicon Piesoresistive pressure scanners
EES	Engineering Equation Solver
CFD	Computation Fluid Dynamics

SUMMARY

The ultimate objective of this research is to investigate the effectiveness of cathode gas (air) recirculation for the thermal management of a solid oxide fuel cell (SOFC) stack. SOFCs conventionally operate at high temperatures (>600^{o} C); and recovering heat from stack exhaust is critical to improving the stack and system performance. Prevalent approaches implement bulky and expensive high temperature gas-to-gas heat exchangers. Also, ejectors are being investigated for recirculation of the air; however, an ejector with typically large velocity gradients would incur large viscous losses. An alternative recirculation approach is being developed for distributed entrainment via active flow control. The entrainment would allow recuperative thermal mixing to occur that may be more effective than the preceding two approaches. The ultimate goal of this research thrust is to reduce, or even exclude, the need of an air preheater in a SOFC system. The cathode air preheat contributes to a large portion of the cost of a SOFC system. Verifying and demonstrating the efficacy of the Coandă effect has been the initial focus, and positive results have been demonstrated in a test environment from a fluid mechanics standpoint. This has been based upon three stages of experimental development, inclusive of cross-sectional area and activated blowing degrees-of-freedom. Seed thermal testing of the system has demonstrated legitimate thermal mixing capabilities. EES thermodynamic modeling developments confirm that the approach can reduce or even exclude the air preheat. It is concluded that recuperative thermal mixing with this recirculation approach is indeed feasible and has the potential to greatly reduce the cost and efficiency of the SOFC system.

CHAPTER 1

INTRODUCTION

A fuel cell system is made up of many supporting parts (i.e. balance of plant) other than just the fuel cell stack. In order to maximize performance of a fuel cell system for a particular application, the balance of plant must be examined. This research investigates the plausibility of reducing the need for one of the parts of the system, the cathode gas heat exchanger. Active flow control is used in place of the heat exchanger to allow for *in situ* and recuperative thermal mixing. Although, this method was primarily investigated for solid oxide fuel cell (SOFC) air streams, the applied research and technique is applicable to fuel stream recirculation in other high temperature fuel cell systems. This chapter introduces applications of high temperature SOFCs. Next, the components of the fuel cell system will be explained, with greater detail specific to the components that this research improves upon. Other state-of-the-art approaches will be discussed and also compared to this approach. Finally, in the last section a preliminary summation of the findings of the research will be provided.

The second chapter is devoted to describing the experimental test setup and the procedure for running tests. Experimental results for fluid mechanic and thermal testing are presented in the third chapter. Next, an energy and exergy balance is performed and the thermodynamic considerations are discussed. The fifth chapter utilizes the energy balance from chapter four and discusses the performance and economic benefits of why this approach is beneficial for SOFC systems. The sixth chapter contains recommendations for future work based upon the guidance of current key findings.

1.1 - SOFC Applications and Benefits

Many potential applications for SOFC systems exist. SOFCs have applications in many power generation areas including, but not limited to, the following: residential, commercial, industrial, military, and communication. The most probable application is in large-scale generators that would provide combined heat and power for large-scale commercial buildings or secluded residential buildings. For military applications, it is preferable to be able to transport only one fuel source, and SOFCs are being investigated to operate on the military's primary fuel JP-8. Also in remote areas not connected to the grid, SOFCs could be used as the primary power source either for a secluded residence or a communications tower.

SOFC systems have benefits over other fuel cell types. A key benefit of SOFC systems over other fuel cell systems is that the high operating temperature allows for fuel flexibility beyond pure hydrogen. Also, high temperatures allow for the use of a non-precious metal catalyst (often nickel) compared with the precious metal catalyst, platinum, used in a proton exchange membrane fuel cell (PEMFC). The nickel catalyst is less susceptible to contamination compared with a platinum catalyst in a PEMFC. A small concentration of carbon monoxide, less than 100 ppm, in the fuel stream of a PEMFC will quickly degrade the membrane [Larminie, 2003]. Alternatively, carbon monoxide may be a direct or indirect (via the hydrogen shift reaction) fuel for SOFCs. The high temperature cell operation brings many technological challenges such as sealing problems, thermal cycling, and necessitated need for high temperature materials. Additionally, thermal management becomes increasingly rigorous.

1.2 – SOFC Operation

SOFC systems produce power, heat, and water from separated hydrogen fuel and air streams. The main components of the SOFC are the electrolyte, cathode, and the anode shown in Figure 1.2.1. SOFCs operate using an oxide ion-conducting ceramic material as

an electrolyte. The electrolyte is typically made from Yttria (Y2O3) stabilized Zirconia (ZrO_2) or YSZ. At high temperatures (>800°C), Zirconia readily conducts O^{2-} ions [Larminie et al., 2003]. Oxygen atoms are reduced on the porous cathode surface with the electrons produced from the anode reaction. The cathode is typically made from lanthanum-based perovskite materials. The anode is currently made from a cermet of Nickel and YSZ [EG&G, 2004]. The separate anode and cathode reactions on each side of the electrolyte with a hydrogen fuel scenario are shown below:

$$2H_2 + 2\,O^{2-} \rightarrow 2H_2O + 4e- \qquad \text{(Anode)}$$

$$O_2 + 4e- \rightarrow 2\,O^{2-} \qquad \text{(Cathode)}$$

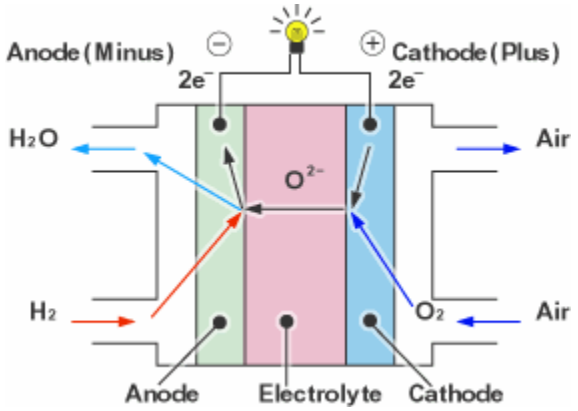

Figure 1.2.1 – Schematic showing the operation of a single solid oxide fuel cell [Seimi Chemical, 2001]

A schematic of the production of electricity in an SOFC is also illustrated in Figure 1.2.1. The reaction of the cathode oxygen, from air, consumes electrons and produces oxygen ions. The product oxygen ion from the cathode reaction conducts through the electrolyte. The electrons travel through an external load producing power. Along with producing electricity, the fuel cell reaction is exothermic. The high operating temperature of the SOFC results in the by-product heat having a large thermal exergy

(i.e., quality). By utilizing this by-product heat instead of expelling it to the atmospheric air, greater system efficiency can be realized. The advanced thermal management approach discussed in this work is an option in managing this by-product heat.

With the electrochemical reactions outlined above a single cell fuel cell has a theoretical open circuit voltage equal to the Nernst potential (e.g., 1 V for a typical SOFC). Figure 1.2.2 shows that the cell potential is related to the current density of the cell through a polarization curve. At the top of the curve where the current density is low and the cell potential is high, activation losses dominate. The source of these losses is from the activation energies of the reactions. The ohmic losses, manifesting as the near-linearity in the middle of the graph, dominate this region and come from electrical contact resistances and material resistivities in the fuel cell. Concentration losses dominate at high current densities and low cell potentials, and these losses are due to mass transfer limitations with respect to the reactants being supplied to the reaction sites.

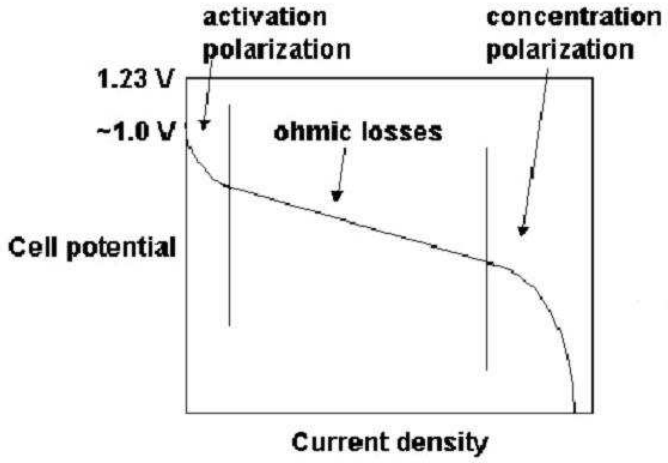

Figure 1.2.2 – Polarization curve for a single fuel cell [von Spakovsky, 2004].

The gases are supplied to the electrodes (anode and cathode) through bipolar plates by way of gas flow channels. The planar design being investigated in this project is a series of single cells connected together and called a stack. An example of an SOFC

stack is displayed in Figure 1.2.3. This is the planar fuel cell stack design to which the proposed thermal management innovation applies. The additional components of the system necessary to operate the fuel cell system are discussed in the next section.

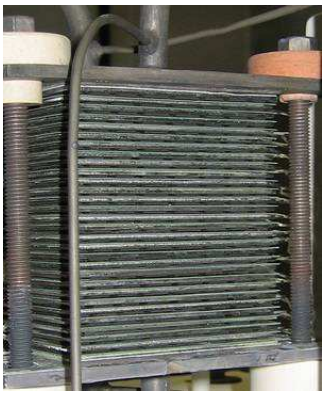

Figure 1.2.3 – Fuel cell stack example [Camtecs, 2006]

1.3 – SOFC System and Advanced Approach

A SOFC system is made up of more components aside from the SOFC stack. The typical system contains an internal fuel reformer, major recuperators (heat exchangers), and blowers/compressors. Figure 1.3.1 displays a schematic of a high temperature fuel cell system. Each component adds to the overall size, weight, and cost of the system.

Two gas preparation subsystems exist in the displayed Figure 1.3.1: the air subsystem and the fuel subsystem. The fuel subsystem contains steam methane reforming and sulfur removal processes to allow for "clean" hydrogen to enter the fuel cell stack. Sulfur will degrade the performance of the system over time; therefore, it needs to be removed. Some SOFC stacks also allow for internal reforming within the stack, but usually this is minimized for thermal management and coking (carbon deposition) concerns. On the air side of the system, the air needs to be preheated to reduce temperature gradients and the corresponding thermal stresses that can be experienced by the stack.

Neither all of the fuel nor all of the oxygen reacts inside the stack. In Figure 1.3.1, the excess fuel is combusted in a tail gas burner to provide some of the heat needed for reforming and for the large air preheater. The proposed alternative would recirculate the exiting cathode air (heated by the by-product stack heat) so that it mixes directly with the incoming air from the blower. A related and future goal of the research is to apply the same concept to recirculating unspent fuel back to the steam methane reformation process. Rather than combusting the exiting fuel, a portion thereof would re-enter the fuel cell stack after passing through the reformer.

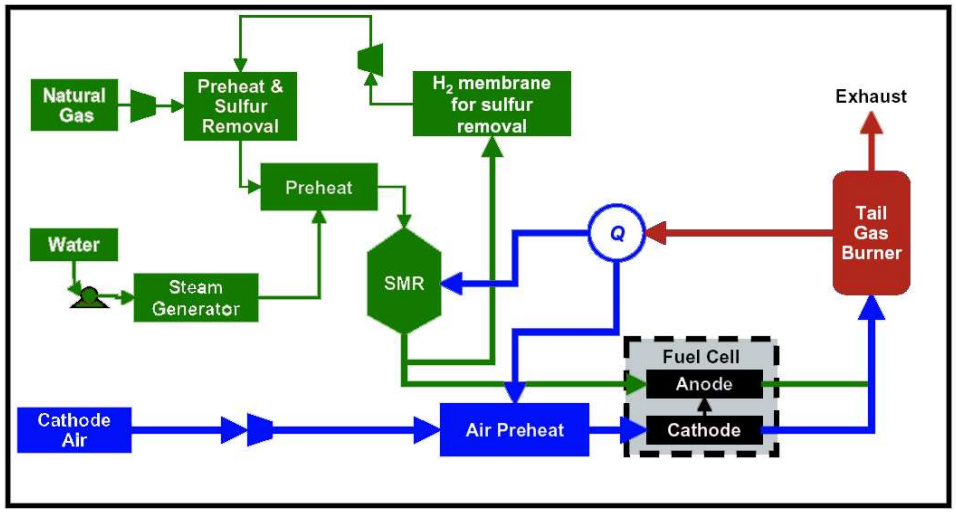

Figure 1.3.1 – Schematic showing some of the components that make up a solid oxide fuel cell system [Agnew, 2004]

At the current phase, this innovation aims to eliminate or reduce the cathode air preheat and reduce the cathode air blower size, weight, and cost. A high temperature gas to gas heat exchanger requires a large component. The large size is due to a low heat transfer coefficient when transferring heat from air to air in comparison to when a liquid is involved. A low heat transfer coefficient necessitates a larger contact surface area for effective heat transfer. The sizes of the different heat exchangers are discussed in the

economic incentives chapter. Figure 1.3.2 gives a representation of the amount of space a recuperator might occupy in a large scale SOFC. If the air on the cathodic side of the fuel cell was not preheated but introduced to the stack directly from the blower, again large thermal stresses would be induced and potentially cause cracks thus increasing already cumbersome sealing problems within the SOFC stack.

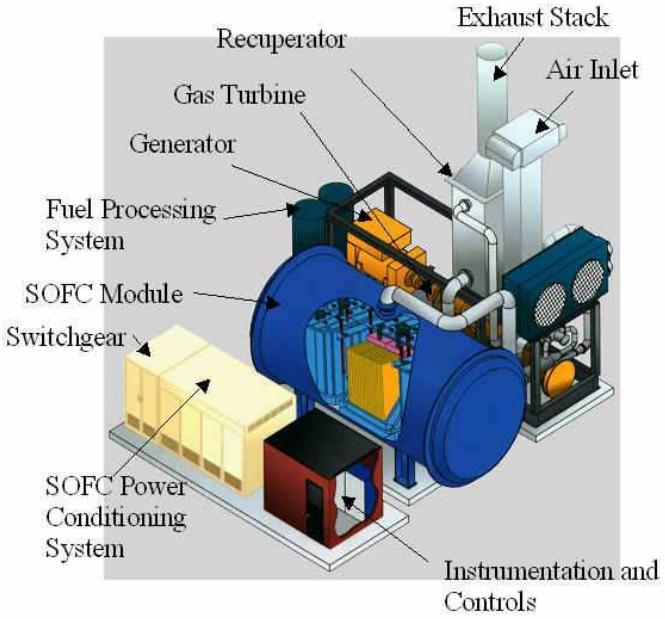

Figure 1.3.2 – Schematic showing some of the components that make up a hybrid solid oxide fuel cell system [NUST, 2006]

The advanced thermal management approach discussed in this thesis has the cathode air exiting the stack mix directly with the air from the blower to preheat the air entering the stack. The heat input into the exiting stack air is generated from the by-product thermal energy of the electrochemical reactions taking place inside the stack. Figure 1.3.3 shows a schematic of the cathodic air circulation associated with this approach. The white squares assigned 1, 2, 3, and 4 are each a potential input jet into the system. Cold air is exiting from the blowers 1-4 and mixing with the heating air throughout the system. The temperature of the entering air thermally mixes with the heated air providing preheated air to the stack.

The input streams entrain and drive the flow in the fluidic circuit. The entering fluid streams thermally mix with the forced re-circulated flow. The mixed streams cause less thermal stress on the system than applying the cold input air stream directly. Input streams 1 and 2 are "upstream" flow controls while streams 3 and 4 are "downstream" flow controls. The surfaces in this figure are shaped to utilize the Coandă effect to drive the flow. The Coandă effect is the tendency of flow over a surface to remain moving in the direction of the surface, useful even in 180^{o} turns. The Coandă effect has mostly been used in the aerospace field in external flows; however, this approach involves internal flow. This effect and the enhancements made to this design utilizing the effect are discussed later in this work.

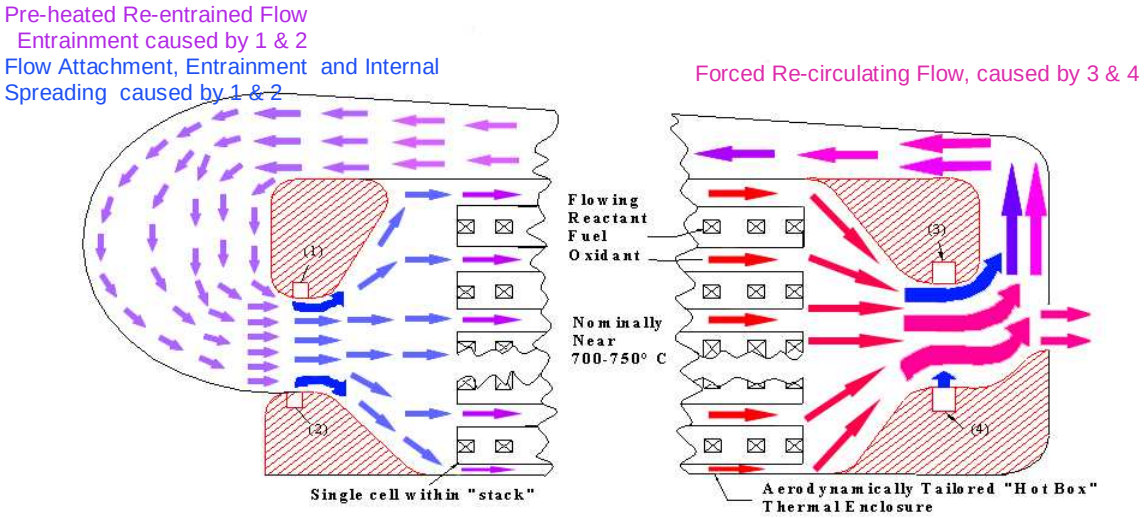

Figure 1.3.3 – Schematic showing the novel advanced thermal management via cathodic air recirculation in a high temperature fuel cell

1.4 - Advanced Thermal Management Utilizing Ejectors

The current technology uses bulky, massive, inefficient, and expensive high temperature gas to gas heat exchangers. The discussed innovation aims to improve upon these downfalls. The relative size of the cathode air preheat was demonstrated in Figure 1.3.2 (ref. the "recuperator" component). Another technology, currently in the

development stages at Rolls Royce Fuel Cell Systems (RRFCS), is using ejectors to recirculate the flow [Agnew, 2004]. The ejector is being investigated in Rolls Royce's 1 MW system [Agnew et. al, 2005]. Figure 1.4.1 presents a schematic representation of an ejector pump implemented in a fuel cell system. The colder incoming air from the blower entrains the high temperature air exiting the stack. The two streams mix thermally inside the diffuser and are expelled at some intermediate temperature.

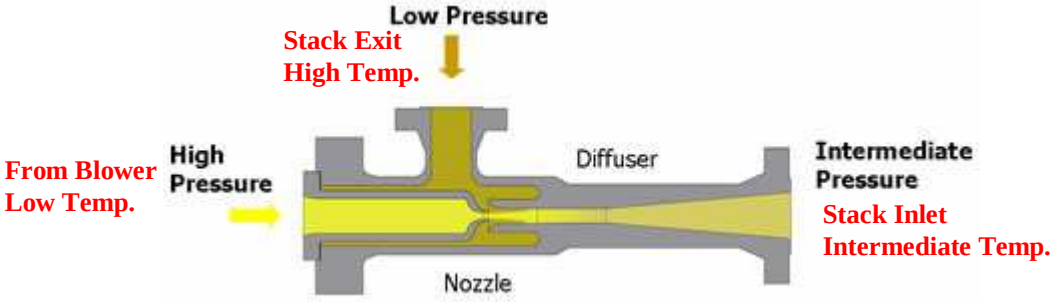

Figure 1.4.1 – Operation of an ejector pump [Transvac, 2006]

Though the ejector design has many benefits over the heat exchanger such as direct heat transfer, it also still contains inherent challenges. Ejectors incur large viscous losses due to the velocity gradients between the low pressure and the high pressure flow. Ejectors are limited in efficiency, since almost all of the momentum transfer between streams is through viscous forces [Jeter, 2005]. Ejectors also represent complexity via another component being added to the system.

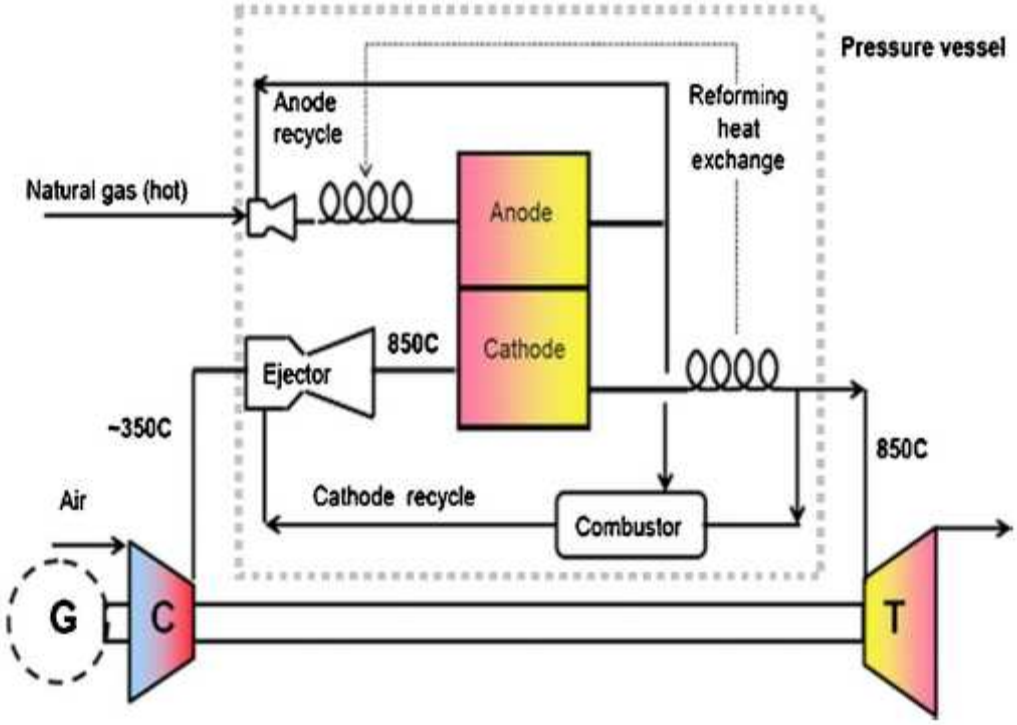

Figure 1.4.2 – Rolls Royce Approach - SOFC system with an ejector pump used for recirculation [Agnew, 2005]

Directly from the continuum methalpy equation it can be shown that in adiabatic steady state flow, the methalpy (h^*) can only be changed by viscous action as shown in equation 1.4.1:

$$h^* = \text{enthalpy} + \text{kinetic energy} + \text{potential energy}$$

$$\rho \frac{Dh^*}{Dt} = -\Delta \bullet q + \frac{\delta P}{\delta t} + V \bullet (\Delta \bullet \tau'_{ij}) + \Phi$$

where if the system is adiabatic, $\Delta \bullet q = 0$

the system is in steady state, $\frac{\delta P}{\delta t} = 0$

$$\rho \frac{Dh^*}{Dt} = V \bullet (\Delta \bullet \tau'_{ij}) + \Phi \qquad (1.4.1)$$

Where ρ is density, t is time, P is pressure, q is the heat input, V is the velocity vector of the fluid, $\Delta \bullet \tau'_{ij}$ is the gradient of the viscous stress, and Φ is the local volumetric

heating due to viscous dissipation. In an ejector, energy exchange between the high pressure and low pressure steam is governed only by viscous action which inherently causes losses in exergy and gains in entropy.

One potential advantage that the presented approach has over the ejectors is that lower velocity gradients may be realized with multiple supply points, reducing the viscous losses incurred. The viscous dissipation is proportional to the square of the velocity gradient from the energy equation for hydro-dynamically fully developed pipe flow [Maynes and Webb, 2004]:

$$\Phi = \mu(\frac{du}{dy})^2 \tag{1.4.2}$$

where μ is the dynamic viscosity and $\frac{du}{dy}$ is the velocity gradient in the radial direction. It is hypothesized, that multiple supply points would provide lower velocity gradients compared to a single supply point, such as an ejector. Another benefit of the presented approach is that it can be included *in situ* within the stack; thus, it does not necessitate another component explicitly aside from the stack, as with an ejector.

1.5 – Summation of Research Findings

The following thesis discusses the findings of the experimental and analytical analyses of this advanced thermal management approach. It is illustrated that the air preheater can be excluded with sufficient addition of the *in situ* thermal mixing approach. Furthermore, initial thermal seed experimentation and analysis show that the hot air exiting the cathode of the stack can be recirculated and thermally mixed with the supplied air *in situ* before re-entering the inlet to the cathode. The Engineering Equation Solver (EES) analysis, based on an energy balance, confirms that the system is capable of excluding the cathode air preheat with thermal mixing. This thermal mixing allows for lower thermal stresses on the stack and also the reduction or exclusion of the expensive gas to gas heat exchanger. With the exclusion of the cathode air preheater, the cost,

weight, and size of the system may be significantly reduced. The details of these research findings are discussed throughout this work.

CHAPTER 2

EXPERIMENTAL SETUP

The experimental setup used for the initial feasibility investigation of the thermal management design was initially built for testing the fluid mechanics of the air. After fluid mechanic feasibility was confirmed, the experimental setup was fit with a thermal stack to determine if it was possible to thermally mix the air *in-situ*. The following subsections will describe the system setups, the different components, data acquisition procedure and equipment, and alterations that were applied to the system.

2.1 – Stack Replica

The original stack replica was intended to provide a nominal partial blockage and to be comparable in flow characteristics (i.e. pressure drop, laminar flow, channel hydraulic radius) to a "typical" industry fuel cell.[1] The cardboard replica is shown in Figure 2.1.1 and in red in all other figures in this document. In later thermal testing, the revised stack replica, shown in Figure 2.1.2, was made of aluminum to allow for a simulation inclusive of heat transfer.

Table 2.1.1 compares each of the stack replicas to a 5 kW stack used by Ceramatec. The diameter of the aluminum stack replica holes could not be reduced due to the need for in-house machining. The velocity of the air flow through the stack for the aluminum stack replica is closer to the velocity of the actual air flow in the Ceramatec stack. At the temperatures tested, the Reynolds number in the channels for both of the stack replicas was much larger than the actual Reynolds quoted by Ceramatec

[1] Although marginally successful as a first trial, an immediate follow-on was the production of another replica for higher fidelity simulation of "real world" stack thermal-fluid behavior.

[Hartvigsen, 2006]. However, the Reynolds number does stay in the laminar flow regime for each of the stack replicas.

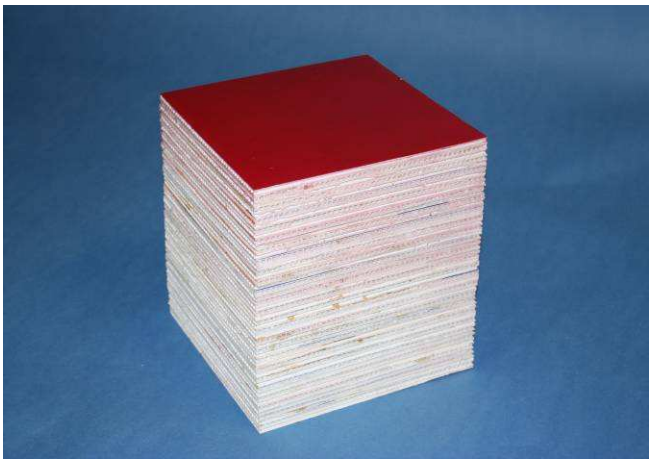

Figure 2.1.1 – Stack replica used for testing the fluid dynamics

Figure 2.1.2 – Aluminum thermal stack replica used for testing the thermal mixing properties

Table 2.1.1 – Comparison of the characteristics of the two stack replicas to those provided by Ceramatec [Hartvigsen, 2006]

	Ceramatec's Actual Stack	***Cardboard Stack Replica***	***Thermal Stack Replica***
Electro-Active Area, (in^2/cell)	50.2	64	64
Frontal Area, in^2	42.3	64	64
Hydraulic Diameter (in.)	0.05248	0.1514	0.375
Velocity (ft/s) with 40 SCFM of air	8.604	4	7.619
Re (channel at 40SCFM)	26.40	310.19	1104.35
% Area Blockage	Not Known	60%	79%

Figure 2.1.3 displays the Reynolds numbers of the cardboard stack and the thermal stack at different operating temperatures. NOS ("number of stoich's") is defined as the ratio of moles of air supplied to the stack to the moles of air needed for stoichiometric electrochemistry, shown in equation 2.1.1:

$$NOS_{\text{sup }plied} = \frac{\text{moles of air supplied to the stack}}{\text{moles of air required by stoichiometry}} \qquad (2.1.1)$$

A more detailed calculation of NOS is presented in Appendix A. The data point shown for the Ceramatec stack is for a 5 kW fuel cell operating at 800^{o}C and a NOS of 8 [Hartvigsen, 2006]. Although, the Reynolds number is larger for both stack replicas, it does remain in the laminar region (e.g. below 2100 for internal flow) [Munson et al., 2002]. Some tests used for characterizing the fluid mechanics and the thermal mixing were conducted at higher turbulent Reynolds numbers than presented here, but those tests had excessive NOS values and were conducted for exploratory testing.

When designing the thermal stack, the diameter of the flow channels was limited by the ability to machine the channels efficiently. Graphically, it is shown that increasing the stack temperature reduces the Reynolds number. The maximum temperature of the stack was limited by the existing experimental setup. In order to implement a more scalable setup (lower Reynolds number) with sufficient NOS, the flow channels must have smaller internal diameters and the setup must be insulated for and operated at a higher temperature. Implementing a fluid other than air with a larger dynamic viscosity may also help in reducing the Reynolds number. These changes are a recommendation for future work. The presented results in this thesis encompass exploratory seed studies.

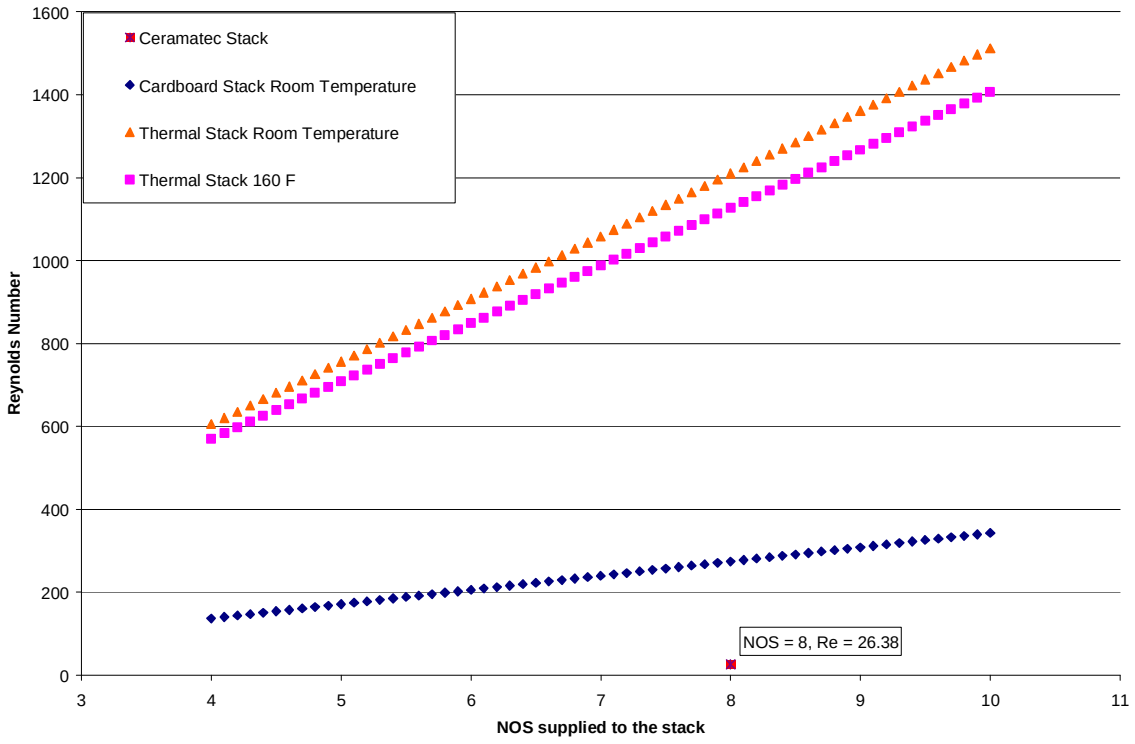

Figure 2.1.3 – Reynolds number as a function of NOS in the experimental stack replicas compared against a Ceramatec stack's Reynolds number (Note: Turbulent Regimes were experienced at higher NOS values during exploratory testing)

2.2 Test Rig Components

Fig. 2.2.1 is a "top view" of the test rig. Seen upstream and downstream of the stack replica in Figure 2.2.1 are two total pressure rakes. These rakes acquire the total pressure at 9 locations across the "tunnel" (i.e., replicated stack enclosure) to get a measure of the flow distribution. Along with static pressure taps located on the top side of the tunnel, the mass flow through the stack can be computed from resolved dynamic pressures. This calculation is discussed in more detail in Section 2.8 "Data Reduction." Three plenums provide a high velocity air flow to the tunnel via the upstream and downstream "Coanda blowers", as well as an "exit area" blower near the vent/purge (i.e., top left of the figure). This air flow then entrains the slower flowing air through the tunnel and drives the flow. A picture of one of the plenums ("Exit Area Plenum") partially disassembled is displayed in Figure 2.2.2. In this thesis, the three plenums are referred to as the exit area, upstream, and downstream blowers or plenums. The exit slots can be adjusted to different widths to alter the velocity of air leaving the plenum. The total pressure in each plenum is recorded to determine the velocity entering the tunnel. The air supply is connected to the bottom of each of the three plenums.

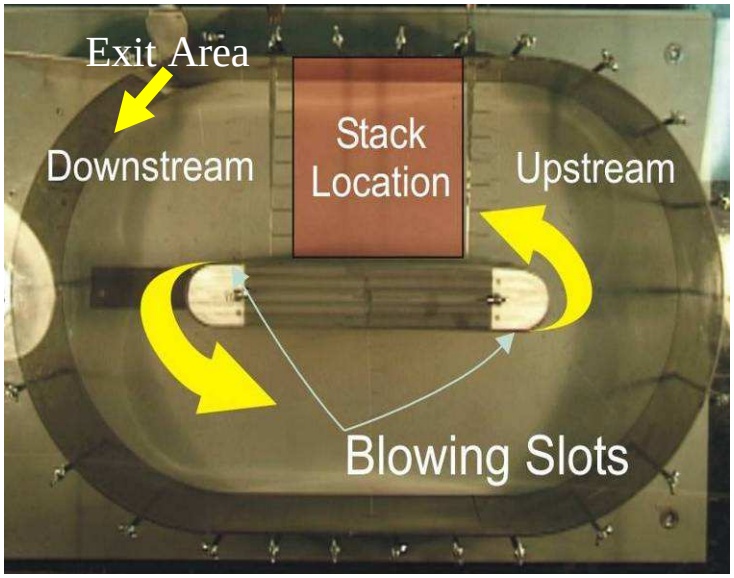

Figure 2.2.1 - Test setup showing the different components of the systems

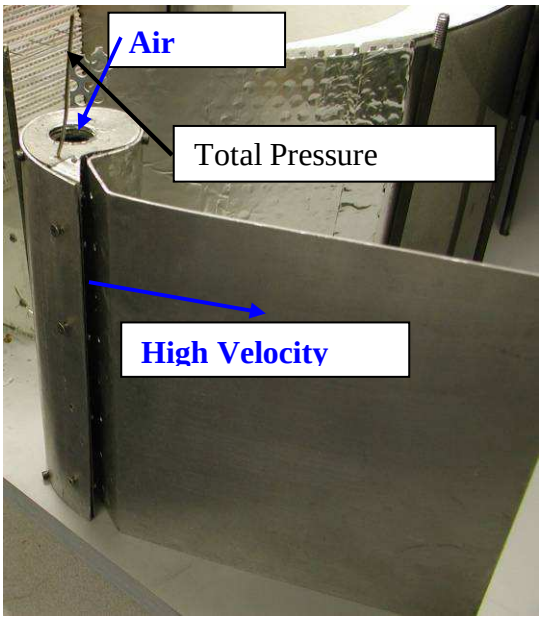

Figure 2.2.2 – Detailed photograph of the exit area plenum assembly

The air supply that drives the flow is provided via critical flow nozzles (CFNs) and is controlled with electronic valves. The flow nozzles are shown in Figure 2.2.3. The air supply is then attached underneath the tunnel shown in Figure 2.2.1 with ¾ inch rubber tubing. Steel piping routes the air to plenums made from sheet metal. Two plenum air supplies are shown in Figure 2.2.1 with the large yellow arrows displaying the incoming air. The air supply subsystem is discussed in further detail in the next subsection.

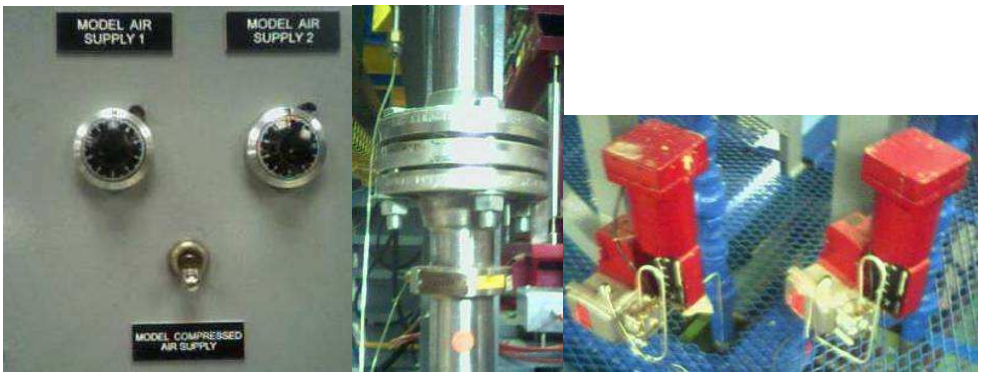

(a) (b) (c)

Figure 2.2.3 – Pictures of the critical flow nozzle: a.) Control b.) CFN c.) Electronic Valves

2.3 – Air Supply System

Air is supplied from a compressor. A schematic for how the air is controlled and supplied to the fuel cell tunnel is shown in Figure 2.3.1. Electronic valves control the mass flow of air supplied to the critical flow nozzles (CFN). By taking a static pressure reading upstream and downstream of the CFNs, the mass flow rate can be determined. The air is then supplied to the plenums by the ¾ inch rubber tubing. The plenum provides air that entrains the flow circulating through the tunnel. The electronic valves upstream of the critical flow nozzles can be adjusted to alter the mass flow of air supplied to the system. With the two supply lines, the system is limited to two degrees-of-freedom regarding plenums blowing at any one time. During experimentation the flow rates were varied between the different blowers.

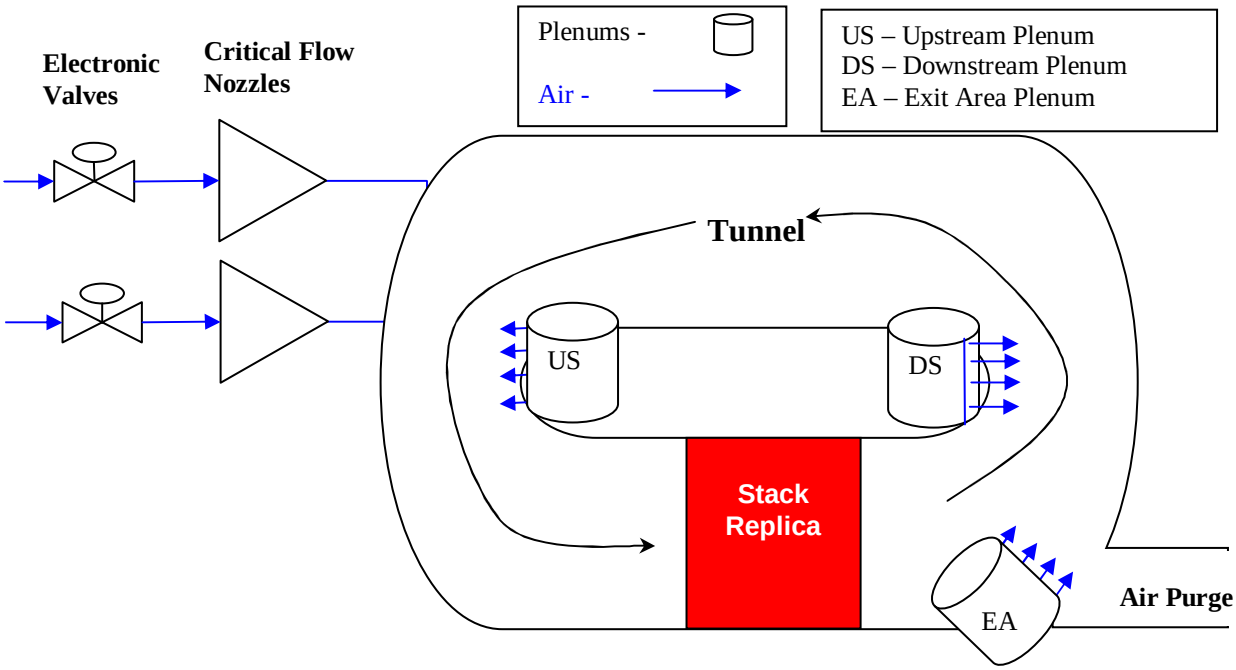

Figure 2.3.1 – Schematic of the air supply system to the testing tunnel

2.4 – Pressure Acquisition

The "brain" of the acquisition system is the Parallel Processing Pressure Acquisition System (Pressure Systems System 8400). The system is equipped with a servo-controlled pressure calibrator. This allows for automated calibration of all of the pressure measurements. The pressure acquisition points shown in Figure 2.4.1 are all connected to electronic silicon piesoresistive (ESP) pressure scanners which contain an array of silicon piezoresistive pressure sensors. An example of an ESP can be seen in Figure 2.4.2. The ports on the ESP pressure scanners were attached to static or total pressure probes throughout the system.

As stated previously, a pressure is recorded upstream and downstream of the CFNs to calculate input air mass flow rate. Atmospheric pressure is recorded for various calculation needs. Each plenum contained a total pressure probe necessary for calculating the exit velocity. With the plenum total pressure, the downstream static pressure, and the ambient temperature the exit velocity of each plenum is determined. Upstream and downstream of the stack location, a "rake" of nine total pressure probes is installed along with a static pressure tap to determine the average dynamic pressure at each location. These total pressure rakes are displayed in Figure 2.4.3. This dynamic pressure can then be used to calculate the mass flow rate upstream and downstream of the stack. The calculation for this is shown in the "Data Reduction" section.

The total pressure rake pressures and the static pressures were taken with an ESP pressure scanner array with a range of $\pm$1 psig, while the remaining total pressures in each plenum were acquired using an ESP array with a range of $\pm$5 psig. The pressures at the CFNs were taken with a 0-250 psig ESP array. Each ESP array is calibrated every day of testing using the Pressure Systems System 8400, a nitrogen tank at known pressures, and a vacuum pump. This advanced acquisition system made it possible to record all the pressures into the computer seamlessly.

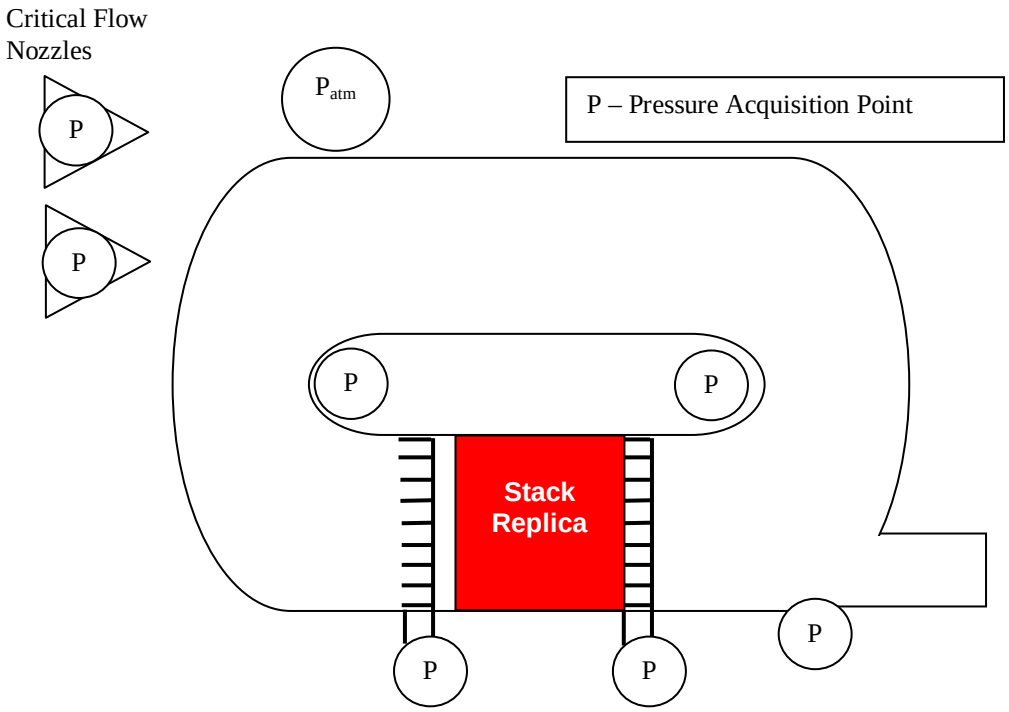

Figure 2.4.1 – Schematic of the pressure acquisition points in the testing tunnel

Figure 2.4.2 – ESP Pressure Scanners

Figure 2.4.3 – Downstream total pressure rake installed into the stack replica channels

2.5 – Thermal System

The far-reaching goal of this project is to determine the feasibility of using the active flow control to thermally manage a high-temperature fuel cell. The initial implementation, a heated stack replica, is displayed in Figure 2.5.1. The thermal stack replica is an aluminum cube, identical in external dimensions to the original cardboard stack replica. Aluminum was chosen for its high thermal conductivity. Resistance cartridge heaters, shown in Figure 2.5.2 are inserted into the aluminum block. The temperature of the block is monitored with thermocouples. The temperature controller along with the cartridge heaters maintains the stack at the desired temperature as air is supplied to the tunnel. A schematic of the thermal setup is displayed in Figure 2.5.3. The temperature controller supplies the necessary power to four 600 W cartridge heaters in order to maintain the stack at a desired temperature. This hot box design is implemented to mimic the byproduct heat that is given off by the electrochemical reactions of the fuel and air. Due to materials limitations in the tunnel (plexi-glass: glass transition temperature 212-221^{o}F (100-105^{o}C), the maximum temperature used for thermal seed testing is 160^{o}F (71.1^{o}C) [MatWeb, 2007]. Due to the heat losses in the setup it is difficult to quantify the extent to which this system can be scaled to 600^{o}C operation. An experimental setup that can withstand higher temperature operation and be able to monitor heat loss would be helpful in determining the scalability of this approach.

With the stack at the desired temperature, multiple temperatures along the tunnel are monitored with K-type thermocouples (Figure 2.5.4). The following locations are monitored: each plenum's input air temperature, the aluminum block in three locations upstream and downstream of the stack replica, and the backside of the tunnel. The temperature is taken in only one location across the width of the setup in each acquisition point due to funding constraints at the time of construction. With the non-uniform velocity distribution (presented in Section 2.9), the non-uniformity of the temperature distribution is almost certain. In order to have a better idea of the temperature distribution, an array of thermocouples should be developed similar to that of the pressure rakes. The thermocouple junctions have a diameter of approximately 0.041 in. to give a conservative response time of 40 ms [Hay et al., 1988]. The temperatures are acquired by an IOTECH Tempscan 1100 temperature scanner. The Tempscan feeds the temperatures to the data acquisition mainframe. These temperatures are then displayed during testing in the LabView™ Virtual Instrument (VI) and saved to an excel spreadsheet for analysis.

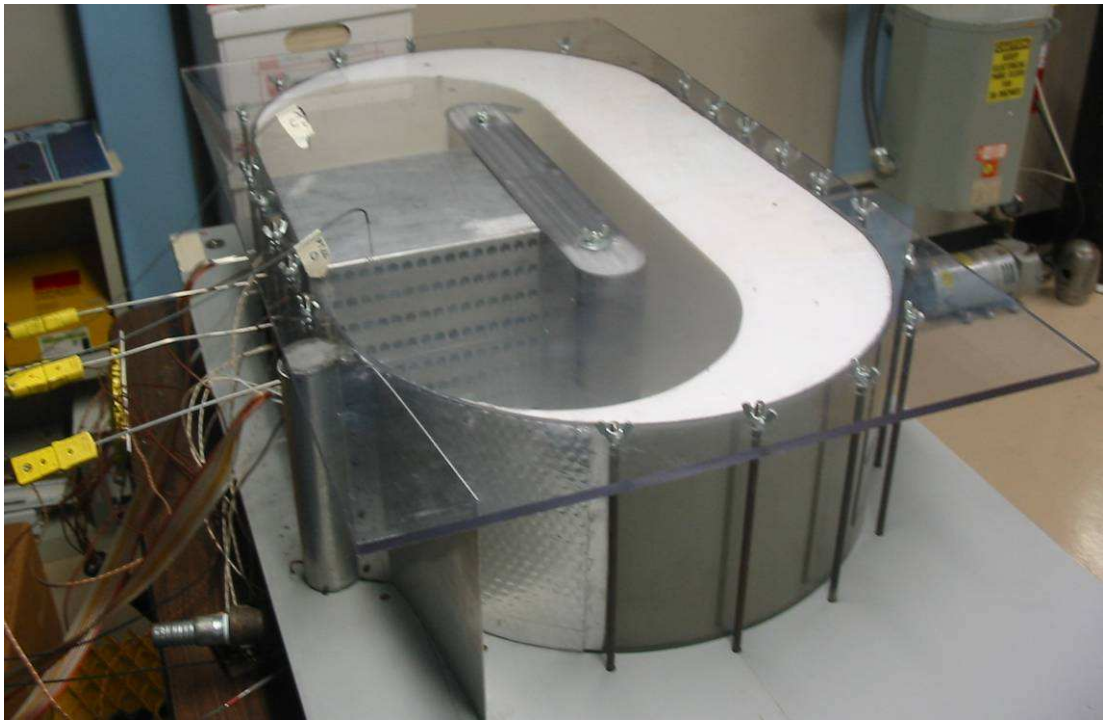

Figure 2.5.1 – Thermal system consisting of the aluminum stack replica used for the initial verification of the Coandă–based thermal mixing approach

Figure 2.5.2 – Cartridge heaters and Omega temperature controller are used to maintain the thermal stack at a constant temperature

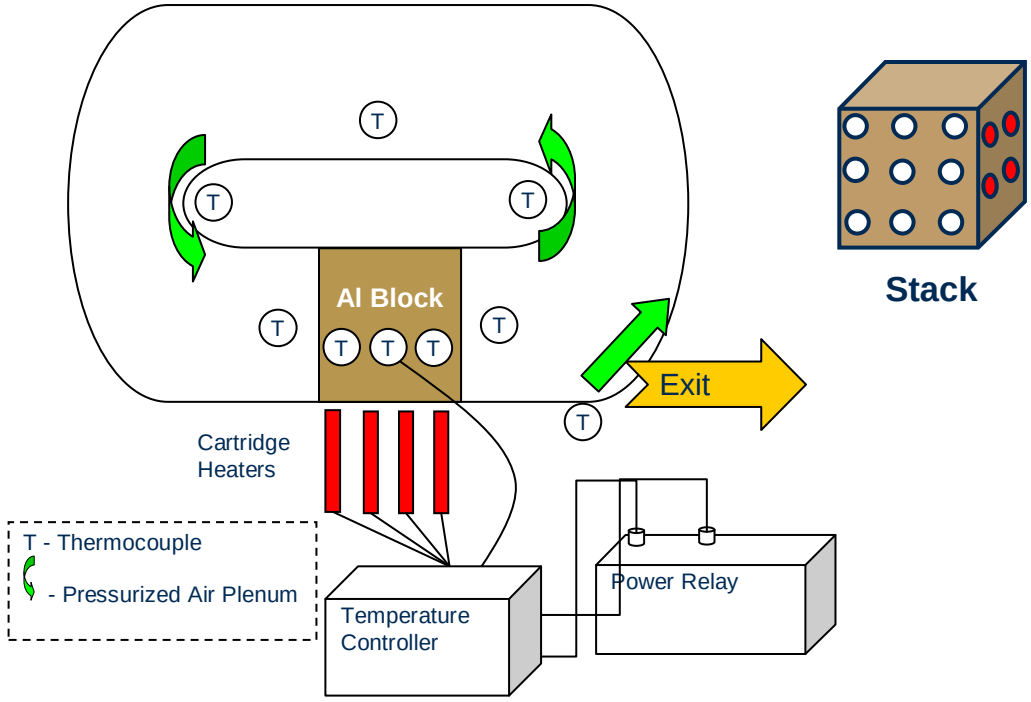

Figure 2.5.3 – Aluminum stack schematic for greater determination of the thermal feasibility of the system

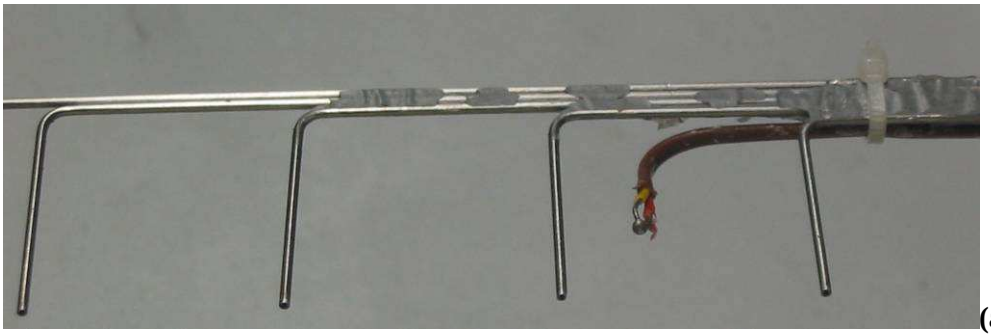

(a.)

(b.)

Figure 2.5.4 – (a.) Exposed K-type thermocouple attached to a total pressure rake, used to monitor the temperatures of the air in the experimental setup in multiple locations

(b.) Sheathed K-type thermocouple used to monitor the aluminum thermal stack temperature at the upstream and downstream locations

2.6 – Calibration and Uncertainty

The pressure system is calibrated using a servo-controlled pressure calibrator. This allows for automatic calibration when the pressure calibrator is connected to the ESP pressure scanner. The calibration box is attached to a nitrogen supply and a vacuum pump in order to ensure the fidelity of the pressure measurements. A Labview™ program is used to automate the calibration process.

A measurement uncertainty analysis has been performed with the key metric being recirculation ratio. The recirculation ratio is a measure of the mass of air circulating through the stack compared with the mass of the supplied air through the plenums. The recirculation ratio is discussed in detail later in this thesis. The

measurement uncertainty analysis was performed using propagation of uncertainties [Figliola et al., 2000]. The calculation of the measurement uncertainty analysis of the recirculation ratio is included in Appendix B. The overall measurement uncertainty of the recirculation ratio was calculated to be 0.9 (16%) for the original cardboard stack and 0.4 (7.3%) for the thermal aluminum stack at a recirculation ratio of 5.5. The majority of the uncertainty was coming from the uncertainty in blockage area for the cardboard stack. With the thermal stack, the uncertainty propagates from total pressure measurements. The measurement uncertainty is reasonable for displaying accurate trends in the data described in the experimental results.

Also, statistical uncertainty was evaluated, since it is valuable in determining the actual precision error of a particular measurement. The statistical uncertainty is most useful when evaluating trends. When investigating the recirculation ratio for a sample of 25 points, the sample standard deviation, S_R, of the recirculation ratio was 0.15. Assuming the data follows a normal distribution, for a confidence interval of 95%:

$$95\ \%\ \text{confidence interval} = \pm 1.96 \bullet S_x$$

This provides a statistical uncertainty, U_R, at 95% confidence of $\pm$ 1.96*.15 or $\pm$ 0.30. The statistical uncertainty, U_{T^*}, for the thermal mixing ratio, T^*, also discussed later, using the same methodology was found to be $\pm$ 0.032. In the experimental plots presented in Chapter 3, the error bars that are shown relate to the statistical uncertainty.

2.7 – Data Acquisition

Data acquisition is performed using the Pressure Systems System 8400 and the IOTECH Tempscan 1100. The data is then transmitted to the National Instruments NI-SCXI 1001 data acquisition mainframe. Labview^{TM} is used as a VI to observe, reduce,

and export the data to a spreadsheet. A screenshot of the virtual instrument is displayed in Figure 2.7.1. The virtual instrument reads the data from the data acquisition mainframe, presents the data in real-time, and performs many of the necessary data reduction steps for further analysis.

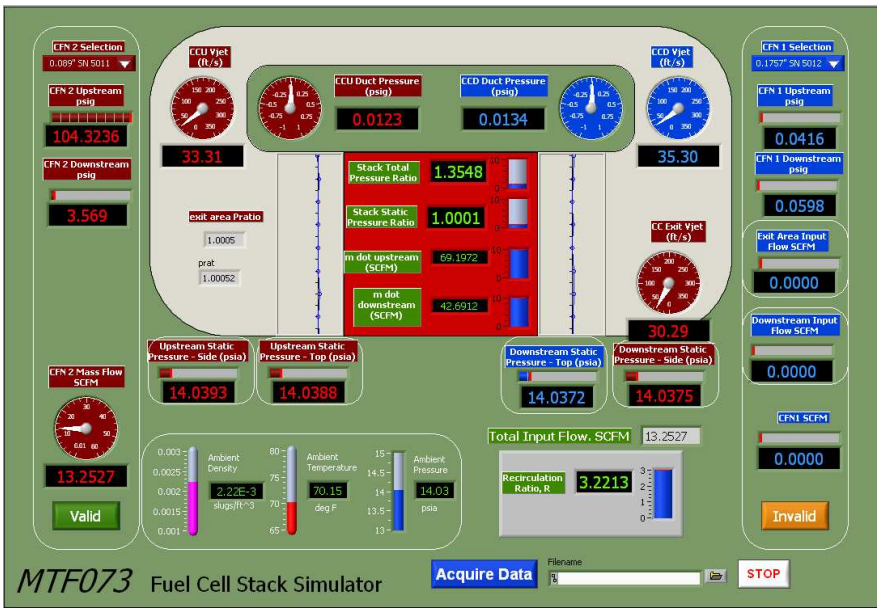

Figure 2.7.1 – Labview™ Virtual Instrument for monitoring, reducing, and collecting data.

2.8 – Data Reduction

As stated in the previous section, much of the data reduction is performed through the Labview™ Virtual Instrument. When investigating the fluid dynamics of the test rig, the most important calculation is the recirculation ratio, R. This was defined as the following:

$$R = \frac{\dot{m}_{\text{air,circulated}}}{\dot{m}_{\text{air,externally supplied}}} \tag{2.8.1}$$

where $\dot{m}_{\text{air,circulated}}$ is the mass flow rate of air through the stack, determined from the downstream total pressure rake and the downstream static pressure tap, and $\dot{m}_{\text{air,externally supplied}}$ is the total mass flow rate of air input through the plenums, determined from the upstream and downstream pressures at the critical flow nozzles. To determine $\dot{m}_{\text{air,circulated}}$ equations 2.8.2 - 2.8.6 were used. Since the total pressure measured by the rake is the sum of the dynamic pressure, P_{dyn}, and the static pressure, P_{stat}, equation 2.8.2 is realized.

$P_{tot,avg}$ = Average pressure (absolute) measured from the 9 total pressure taps
P_{stat} = Static Pressure (absolute) measured at the pressure tap location
A = Open area at total pressure acquisition location

$$P_{dyn} = (P_{tot,avg} - P_{stat}) \tag{2.8.2}$$

$$P_{dyn} = 1/2\rho v^2 \tag{2.8.3}$$

$$v = \sqrt{\frac{2P_{dyn}}{\rho}} \tag{2.8.4}$$

where v is the velocity and ρ is the density calculated using the ideal gas law:

$$\rho = \frac{P_{stat}}{R_{air} \cdot T_{air,DS}} \tag{2.8.5}$$

where R_{air} is the gas constant for air and $T_{air,DS}$ is the ambient temperature at the downstream pressure tap location. Then it follows that:

$$\begin{aligned} \dot{m}_{lb/s} &= \rho \cdot v \cdot A = [lb/s] \\ \dot{m}_{air,circulated,SCFM} &= 783.9 \cdot \dot{m}_{lb/s} \end{aligned} \tag{2.8.6}$$

The $\dot{m}_{\text{air,externally supplied}}$, can be calculated from the critical flow nozzles as seen in equation 2.8.7 [Flow-dyne, 2006].

$$\dot{m}_{air,externally\,supplied} = \frac{c_1 P_{inlet}{}^3 + c_2 P_{inlet}{}^2 + c_3 P_{inlet}}{60\sqrt{T_{amb}}} \tag{2.8.7}$$

where c_1, c_2, c_3 are all constants for the specific flow nozzle, P_{inlet} is the inlet pressure to the CFN, and T_{amb} is the ambient temperature of the entering air. Recirculation ratio is a critical metric from a fluid mechanics standpoint. The results from the experimentation are discussed in the next chapter "Experimental Findings and Discussion".

2.9 – System Additions and Alterations

With the initial test rig, after achieving low recirculation ratios, a visualization study was conducted using a fogger. It was seen that large vortices were forming within the tunnel. As the moving air contacted the stack replica, vortices and "backwards flow" were induced, lowering the recirculation ratio. Figure 2.9.1 shows a picture of this visualization study.

The design response was to reduce the cross-section in the back side of the tunnel, where the stack replica is not located. This was accomplished by designing a foam insert to fit the tunnel. A computer aided design graphic is presented in Figure 2.9.2. The completed insert is displayed assembled with the tunnel in Figure 2.9.3. When the foam insert was introduced, the distance between the metal surface and the back wall was reduced. Through experimentation, T. Panitz and D. Wasan of Illinois Institute of Technology discovered the Coandă effect to cause less flow inhibiting vortices with a smaller distance from this back wall [Panitz and Wasan, 1972]. This concept is discussed in more detail in Section 3.1. With the foam insert implemented, vortices are now only seen upstream of the stack in the visualization study shown in Figure 2.9.3. These vortices upstream of the stack, though unfavorable to the fluid mechanics, may have a beneficial thermal mixing effect.

Figure 2.9.4 shows the velocity distribution downstream of the stack with the foam insert included. This was not able to be improved upon with the addition of the foam insert. The non-uniformity also implies that the temperature distribution during the

heated tests will most likely be non-uniform. Future CFD studies may be beneficial in designing blowers that produce uniform flow entering and exiting the stack. This will allow for an even temperature and current distribution across the stack. Although it did not correct the uniformity issue, the tunnel cross-sectional area reduction decreased backflow effects.

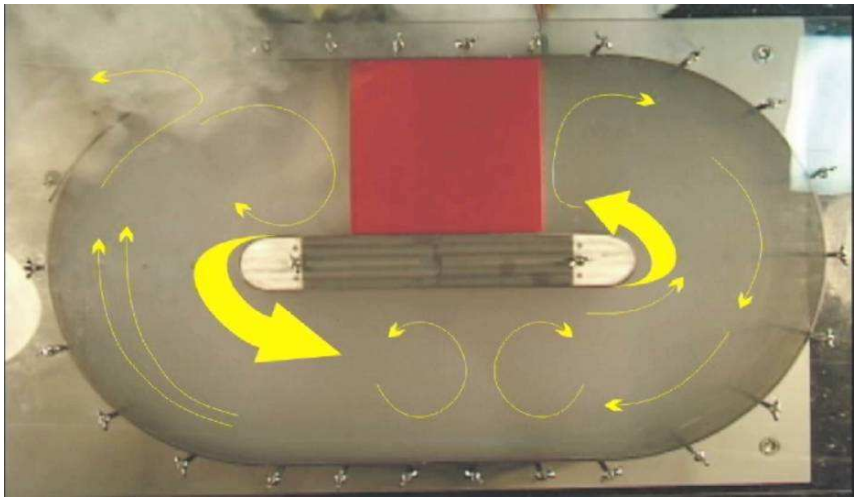

Figure 2.9.1 – Picture of tunnel with smoke visualization showing the vortices and "backwards flow" reducing recirculation

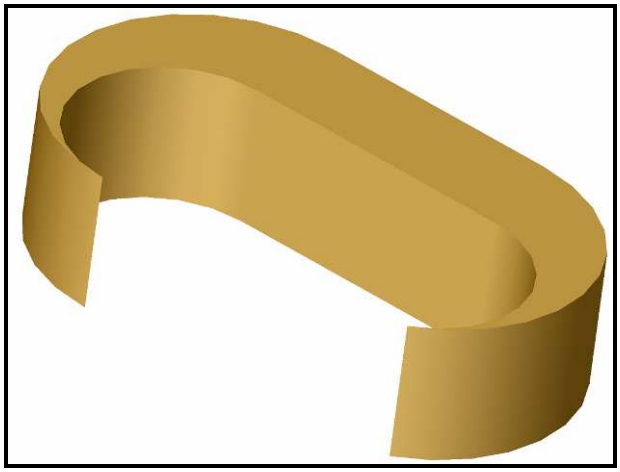

Figure 2.9.2 – Foam insert created to reduce the cross-sectional area of the tunnel

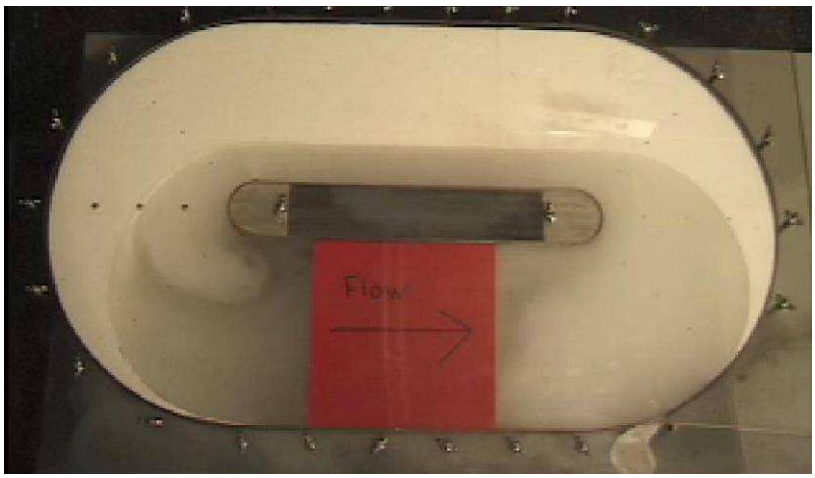

Figure 2.9.3 – Foam insert assembled into the fuel cell tunnel to improve recirculation

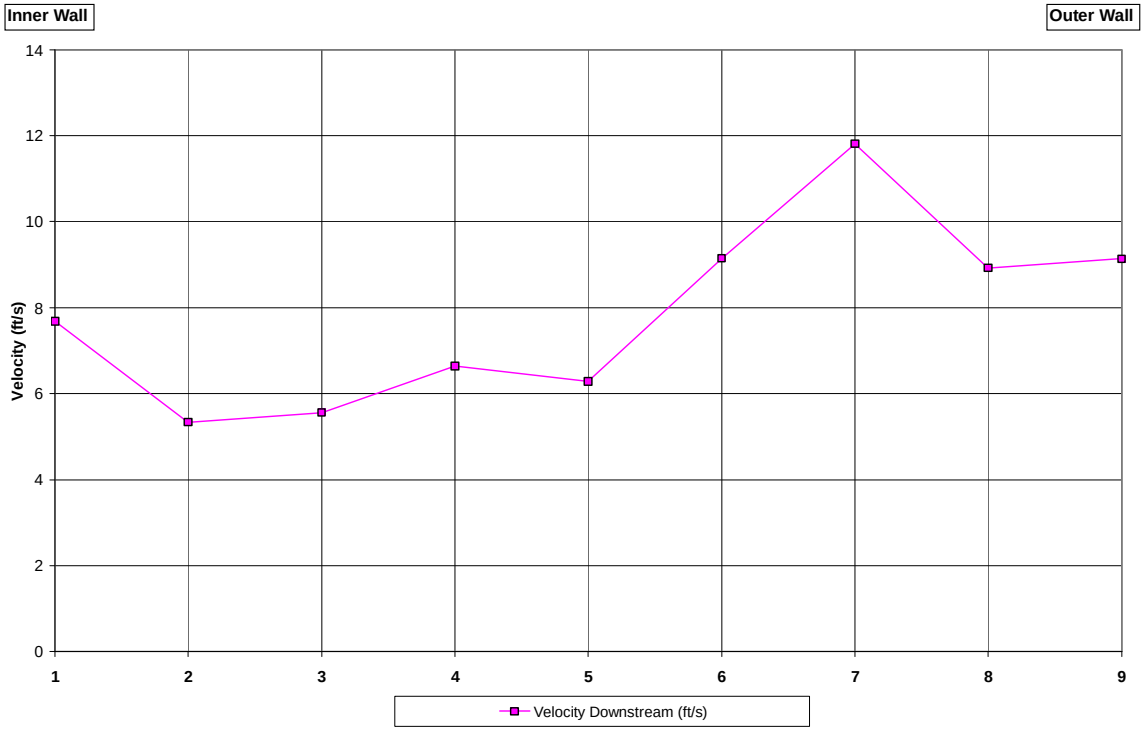

Figure 2.9.4 – Velocity distribution showing the non-uniformity of flow with the inclusion of the foam insert and the exit area blower activated (approximately 81 SCFM through the stack)

The reduced cross-sectional area on the back side of the tunnel slightly altered the Reynolds number of the air flow. However, the flow remained between the transitional and turbulent flow regime at typical NOS values. In the turbulent flow regime a greater deal of thermal mixing of the air is believed to occur due to larger eddies and vortices. Figure 2.9.5 displays the Reynolds number of the flow on the backside of the tunnel and upstream of the stack replica. Larger Reynolds numbers and NOS values were purposely tested in the exploratory experiments presented in the Chapter 3.

With the foam insert included, recirculation was greatly increased, as presented later in "Experimental Findings and Discussion". With the added recirculation induced by the foam insert, the exit area plenum next needed to be investigated. When implementing the exit area plenum, it was noted that the total pressure probe inside the plenum was blocked. This blockage necessitated disassembling the plenum, unclogging the plenum, reassembling, and then resealing the plenum; hence there was a significant delay in project progression. After reassembly, the entrance angle of the blower was changed to approximately 45 degrees from the tangent of the tunnel wall. When this angle was altered, pressurization in the tunnel caused the exit area door to be unstable. To correct this problem, a new aluminum mesh screen door was inserted in the original Plexiglas door's place. With the new door, it was noticed that the air leaving the exit area plenum was attaching to the exit guide causing negative effects on recirculation. The exit door was then attached directly to the plenum to guide the flow away from the exit. A summary of these adjustments is shown in Figure 2.9.6. While the retrofit significantly delayed the project schedule, it brought significant improvements over prior experiments.

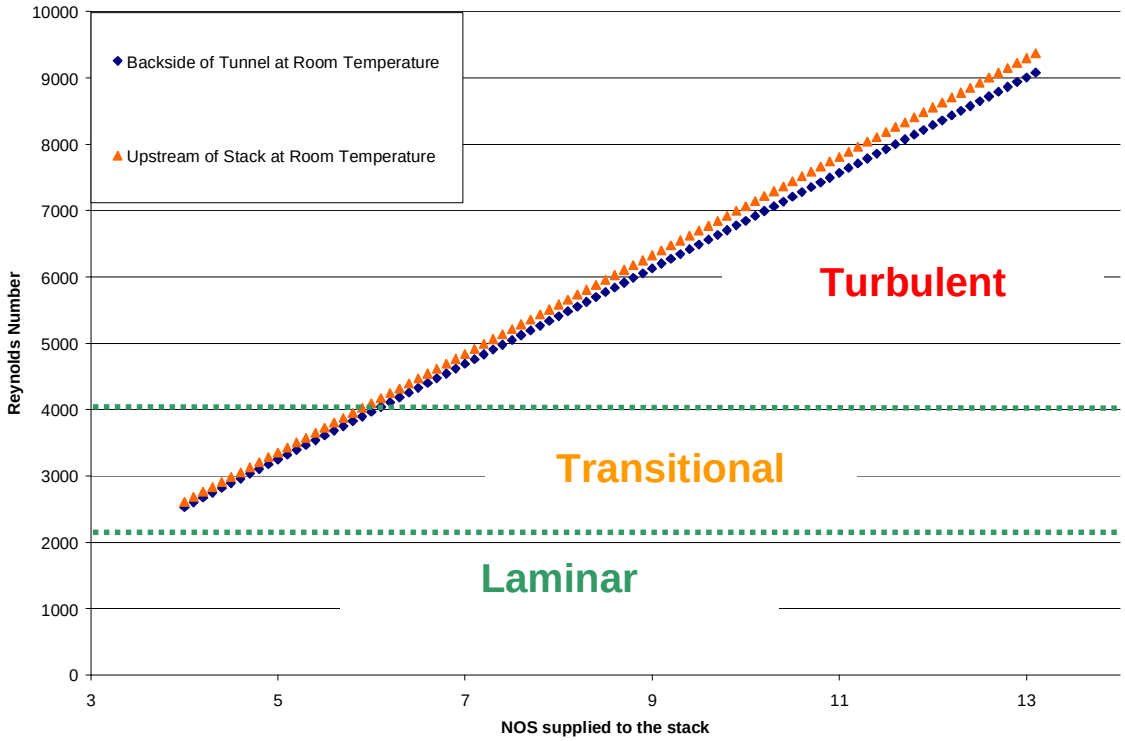

Figure 2.9.5 – Comparative Reynolds numbers at typical NOS values for the experimental setup with the foam insert installed (NOS based on a 5 kW stack)

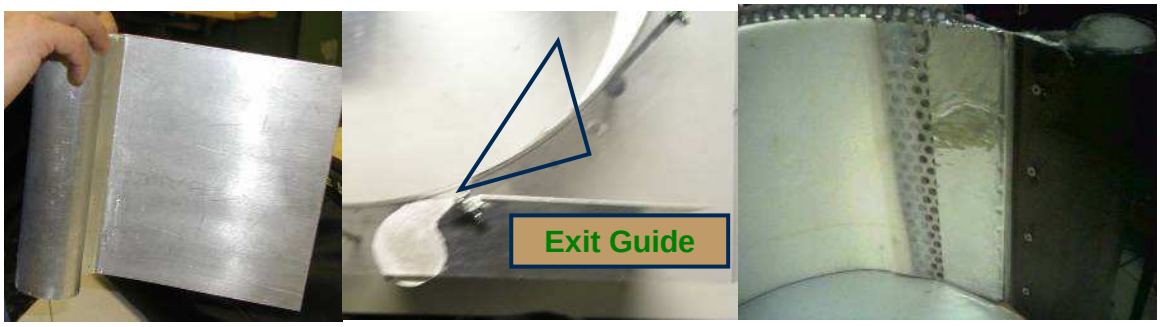

Blower was removed for sealing

Entrance angle was altered (45°)

Flow attachment to the exit guide was precluded

Figure 2.9.6 – Exit area plenum adjustments to improve recirculation

CHAPTER 3

EXPERIMENTAL FINDINGS AND DISCUSSION

Initial experiments testing the upstream and downstream plenums were performed without the stack replica in place. The results for these experiments were used to determine a maximum recirculation ratio that could be achieved with the two blowers, since the flow resistance induced by the stack replica inevitably decreased the system recirculation ratio. Accordingly, once the stack replica was introduced the recirculation ratio greatly decreased.

With the increase in flow resistance at the stack location, the foam filler was then introduced to increase "back flow" resistance on the back end of the tunnel, as described in Section 2.8. The following chapter discusses the modifications made to the experimental setup and their effects on the performance based on recirculation ratio and the thermal mixing ratio, both discussed later.

3.1 – Coandă Effect

The Coandă effect is the phenomenon that flow over a surface tends to stay attached to the surface. As an example, if one places a spoon in a running faucet, the flow will leave the spoon at the angle of the curvature rather than vertically downward. This effect is critical in the design of supersonic flight vessels. The upstream and downstream blowers were both designed to utilize the Coandă effect. The Coandă surface of the blower design is illustrated by the arrow in Figure 3.1.1. The blowers were designed to maintain the supplied flow attached to the sheet metal wall. This attached flow then entrains the rest of the flow through the tunnel.

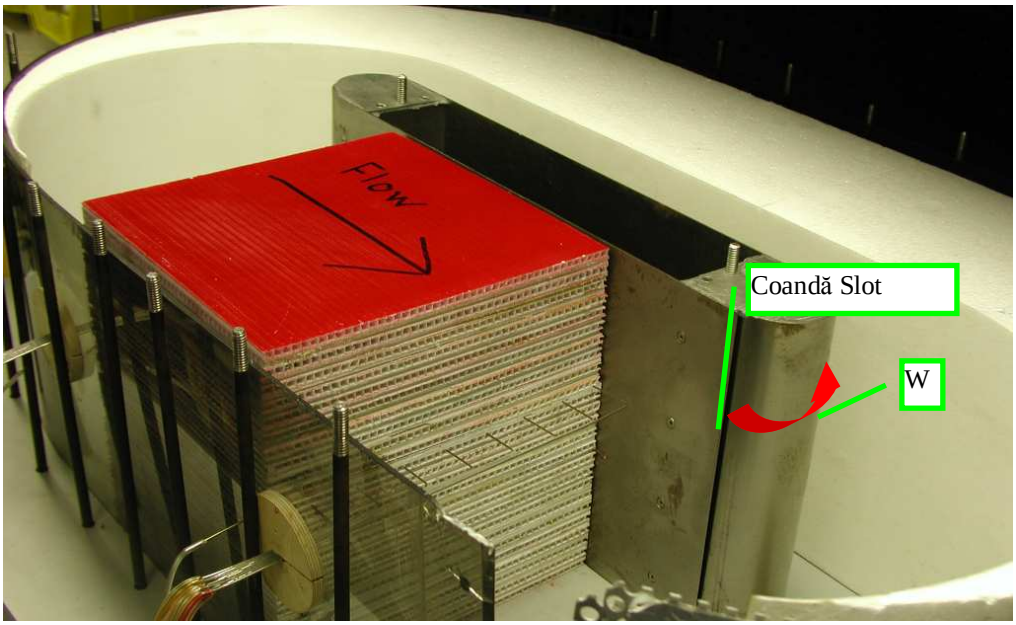

Figure 3.1.1 – Illustration of the design of the Coandă blowers

Prior research shows that entraining flow, with an ejector, while utilizing the Coandă effect is more efficient than without the Coandă effect [Ameri, 1993]. The Coandă effect was seemingly enhanced by reducing the distance between the foam insert and the back metal wall, denoted W in Figure 3.1.1. Before experimentation, a critical confirmation needed for continuing the research was whether the Coandă effect could drive the flow in the given system. After testing, it was discovered that this phenomenon could indeed drive the internal flow of the tunnel. This allowed for the research to progress.

3.2 – Recirculation Ratio Improvements

The baseline experiments did not include the foam insert cross-sectional area reduction (i.e. to the gross passageway). The results of the system without the stack replica versus with the stack replica are displayed in Figure 3.2.1. Once again, these measurements of downstream flow are taken as an average of the flow across the nine pressure measurements from the pressure rake downstream of the stack. The inclusion of

the stack replica provided flow resistance. With this flow resistance, it was evident that the inclusion of the stack replica greatly reduced the recirculation, reducing R to 1 in Figure 3.2.1.[2] From flow visualization studies shown previously in Figure 2.9.1, it was determined that vortices and backflow effects were evident on the backside of the tunnel. These backflow effects were reducing the recirculation inside the system.

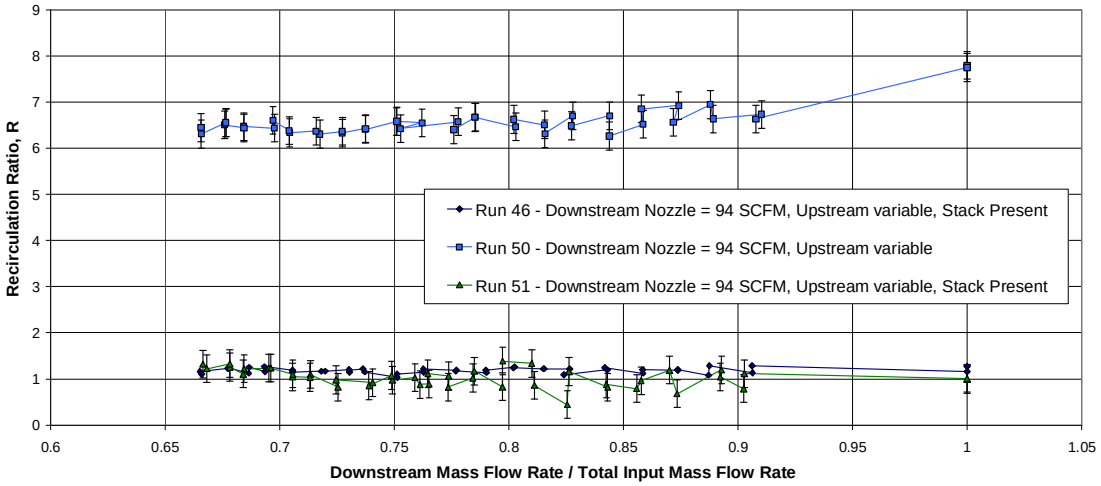

Figure 3.2.1 – Initial results of experimentation without the reduced cross-sectional area using the upstream and the downstream plenums (U_R=±0.30)

To mitigate the vortices and backflow shown in Figure 2.9.1, the foam insert was created to reduce the cross-sectional area of the tunnel. The cross-sectional area reduction brought the recirculation ratio above 2 with the stack present. Conceptually, this is enough recirculation to significantly reduce the high temperature cathode gas heat exchanger. Figure 3.2.2 directly compares the results of the testing with and without the foam insert. With the foam insert, the flow appears to follow a more stable trend with less variation in recirculation ratio due to the vortices. It is shown that the foam insert

[2] The default of all ensuing data graphs is that the stack replica is present.

improved performance in Runs 52 and 53. Also, with the addition of the foam insert, the threshold at which circulation occurs decreases, illustrated in Figure 3.2.3. The threshold described here is the minimum input supply rate at which recirculation occurs. The threshold decreased from an input supply rate of approximately 75 SCFM to approximately 30 SCFM with the foam filler.

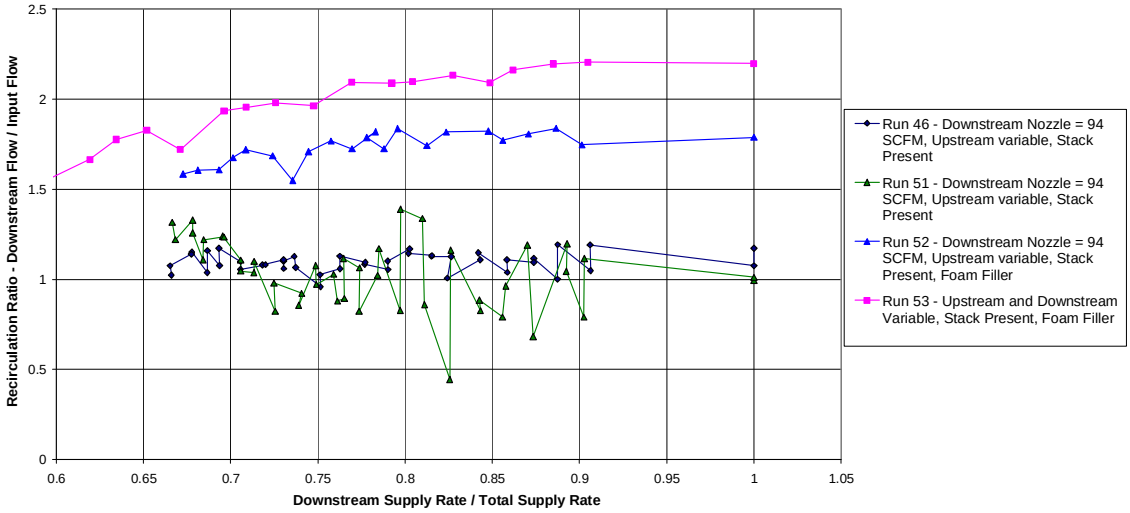

Figure 3.2.2 – Comparison of results with and without the foam insert (U_R=±0.30)

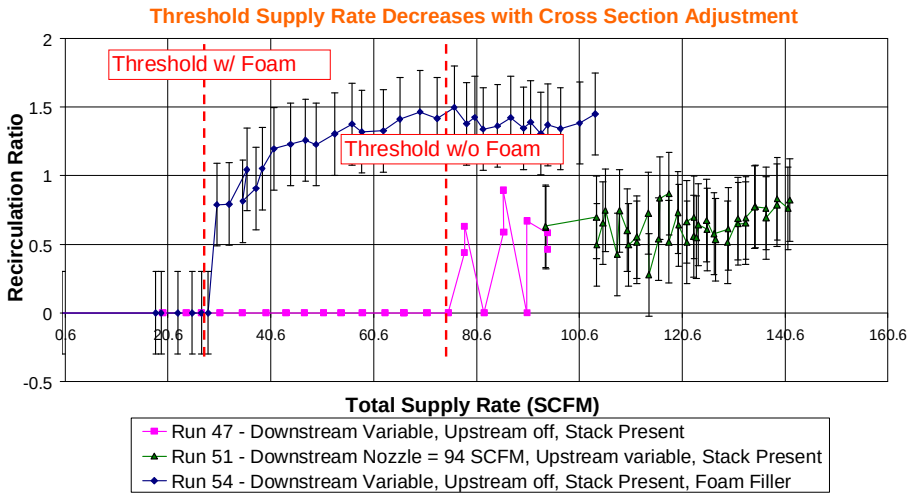

Figure 3.2.3 – The threshold decreases when the cross-sectional area is reduced on the backside of the tunnel (U_R=±0.30)

The refurbishment of the exit area blower allowed for the comparison between the exit area and the downstream blower. It was previously determined that activating a second plenum decreased recirculation, in comparison to exclusively supplying air through one plenum. Figure 3.2.4 shows this trend. As a second blower is activated the recirculation ratio decreases. The blowers may have counteracting effects. A possible explanation of the degrading effects of activating the downstream plenum while the exit area plenum is activated and vice versa is interfering effects. As an example, the exit area blower is designed to entrain the flow towards the outer edge of the tunnel, while the downstream blower is designed to utilize the Coandă effect to entrain the flow along the inner edge of the tunnel. When a second blower is introduced, the hypothesis is that these effects are partially counteracting (e.g., manifestation of *opposing* velocity vector components).

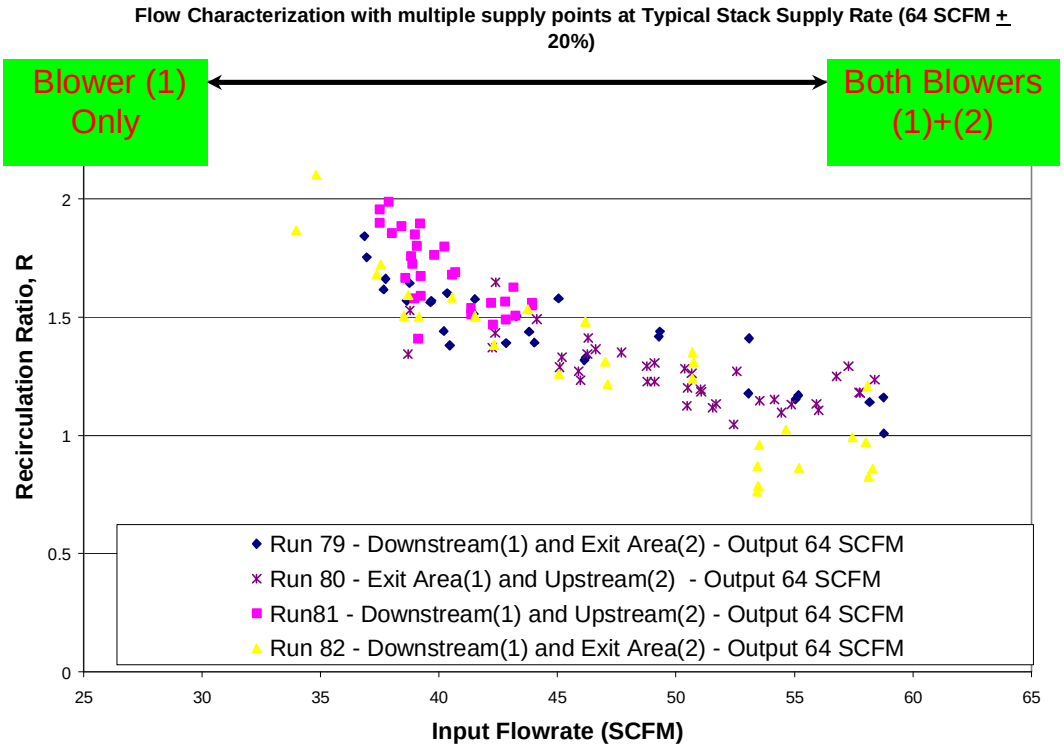

Figure 3.2.4 – Recirculation decreases with the activation of a second blower (U_R=±0.30)

In Figure 3.2.5, three runs were conducted wherein air was supplied via the downstream and exit area slots. Recirculation was tested with different percentages of each blower running. The figure displays that the best recirculation occurred when only the exit area plenum is blowing. The exit area blower was designed to control and limit the amount of air exiting the tunnel through the air purge. Figure 3.2.5 illustrates the effectiveness of the exit area plenum design. However, Runs 79 and 82 show that activating the exit area plenum while the downstream plenum is active actually reduces recirculation. This same trend was found with the upstream blower introduced while the exit area plenum or the downstream plenum was activated. With the current geometry, one blower activated produces the best results. Again the rationale is that the isolated flow fields engendered by the separate blower plenums have opposing vector components at certain locations.[3]

After the refurbishment of the exit area blower, the recirculation ratio maximum of 2.4 with the foam filler significantly increased to a value of 6.1 when using the exit area plenum. The modifications to the exit area plenum are described in greater detail in Section 2.8. The exit area plenum acts similar to a "pneumatic door" that controls the amount of air purged from the system. Flow through the exit area blower creates an air barrier at the purge allowing more significant recirculation in the system. Figure 3.2.5 shows the improvement with the refurbished exit area plenum. Every run in this figure contains the stack replica. In earlier testing, the upstream blower was determined to be inferior in recirculation in the test rig; therefore, it is not included in every figure throughout this chapter. In the EES analysis discussed in Chapter 4, this mediocre ability of thermal mixing is presented. Figure 3.2.6 shows the large progressions from the

[3] Run 84 has multiple points at the zero percent of the input flow coming from the downstream blower, since only the exit area blower was activated in this run. The input flow rate was not constant in Run 84.

introduction of the exit area blower and the cross-sectional area reduction. In addition to significant increases in recirculation ratio, the threshold input supply rate was significantly reduced. The tunnel was able to perform positively at lower input supply rates. This threshold improvement increases the capacity/flexibility of this proposed thermal management approach. With further design improvements to greater utilize the Coandă effect, it is believed greater recirculation could be realized.

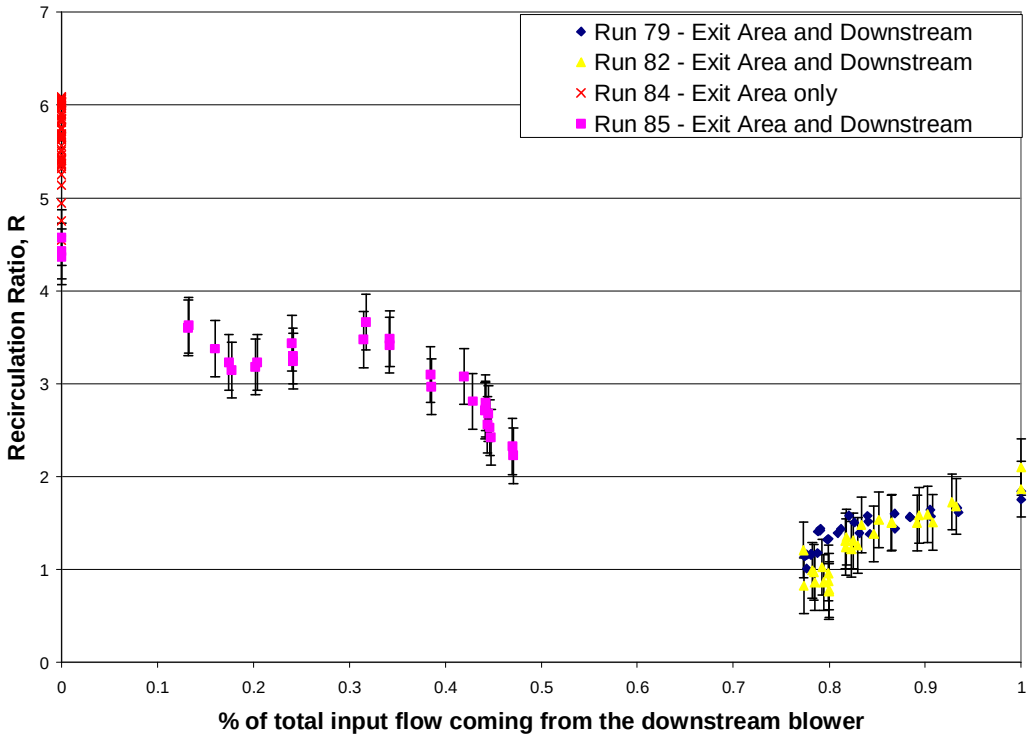

Figure 3.2.5 – Comparing the effectiveness of the downstream plenum to the exit area plenum (U_R=±0.30)

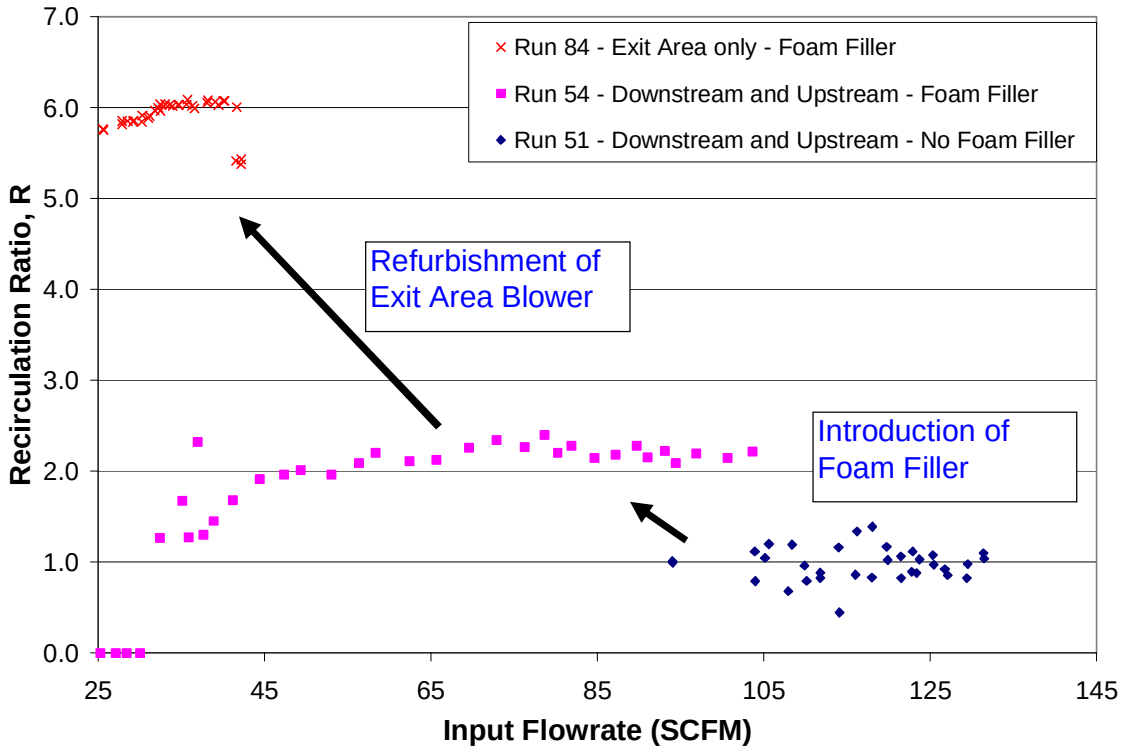

Figure 3.2.6 – Project progression with introduction of the foam insert and the exit area plenum (U_R=±0.30)

3.3 – Thermal Stack Testing Experimental Results

The main scope of this work is to determine if it is feasible to thermally mix the air *in-situ* with the multiple supply point thermal management approach. The addition of heat into the system, *via* resistance cartridge heaters, allowed the determination of the degree of thermal mixing that was occurring in the system. The thermocouples along the test rig allowed the thermal mixing to be quantified. The following results show that indeed it is possible to thermally mix the flow *in-situ* using the multiple supply point approach.

In order to compare between different test runs, and be able to compare to the existing cathodic gas to gas heat exchanger, a temperature ratio quantifying the thermal mixing in the system was developed, T^*:

$$T^* = \frac{T_{air,upstream} - T_{air,inlet}}{T_{stack} - T_{air,inlet}} \tag{3.3.1}$$

where $T_{air,upstream}$ is the air temperature entering the stack, $T_{air,inlet}$ is the air temperature entering into the system from the blower, and T_{stack} is the average stack temperature. This metric is used as a relative measure of how much the air temperature has increased from the inlet air temperature to the stack temperature.

Before heat was introduced into the system, tests were conducted comparing the thermal aluminum stack replica to the initial cardboard stack replica. The results of these tests are included in Figure 3.3.1. As expected, a lower recirculation ratio is seen in the thermal aluminum stack replica than the cardboard stack replica. The aluminum stack is designed with a 79% area blockage compared to approximately 60% area blockage of the cardboard stack. A negative slope is observed when the thermal stack replica is in place. This may be due to increased backflow and vortices with a greater blockage. With a redesign of the foam insert, creating a larger flow resistance on the backside of the tunnel, the backflow and vortices may possibly be mitigated.

When investigating the thermal mixing capabilities, T^* was used to compare between the different blowers and different stack temperatures used. The incoming air was delivered through the plenums at approximately 67^{o}F (19.4 ^{o}C). During multiple tests the stack temperature was maintained at temperatures of 110 ^{o}F (43.3 ^{o}C), 120 ^{o}F (48.9 ^{o}C), 140 ^{o}F (60.0 ^{o}C), and 160 ^{o}F (71.1 ^{o}C). Figure 3.3.2 and Figure 3.3.3 compare the thermal mixing capabilities of the three individual blowing slots at 140 ^{o}F (60.0 ^{o}C) and 160 ^{o}F (71.1 ^{o}C), respectively. These figures show that the exit area blower is capable of more thermal mixing than the upstream and the downstream blower in the experimental setup. Also shown in the EES model discussed in Chapter 4, thermal mixing is more effective if done downstream of the stack (either by the exit area blower or the downstream blower. If the air is introduced in the downstream control volume, it is thermally mixing with both the purge air and the recirculating air at or near the stack temperature. If the incoming air is introduced upstream of the stack, it is mixing with a lower temperature air (e.g., due to dissipative heat losses along the flow path) with less mass flow (no purge air included within the thermal balance). The results also show that

each blower is capable of raising the temperature of the incoming air. This essentially qualifies that recirculation in this system can allow for thermal mixing to occur.

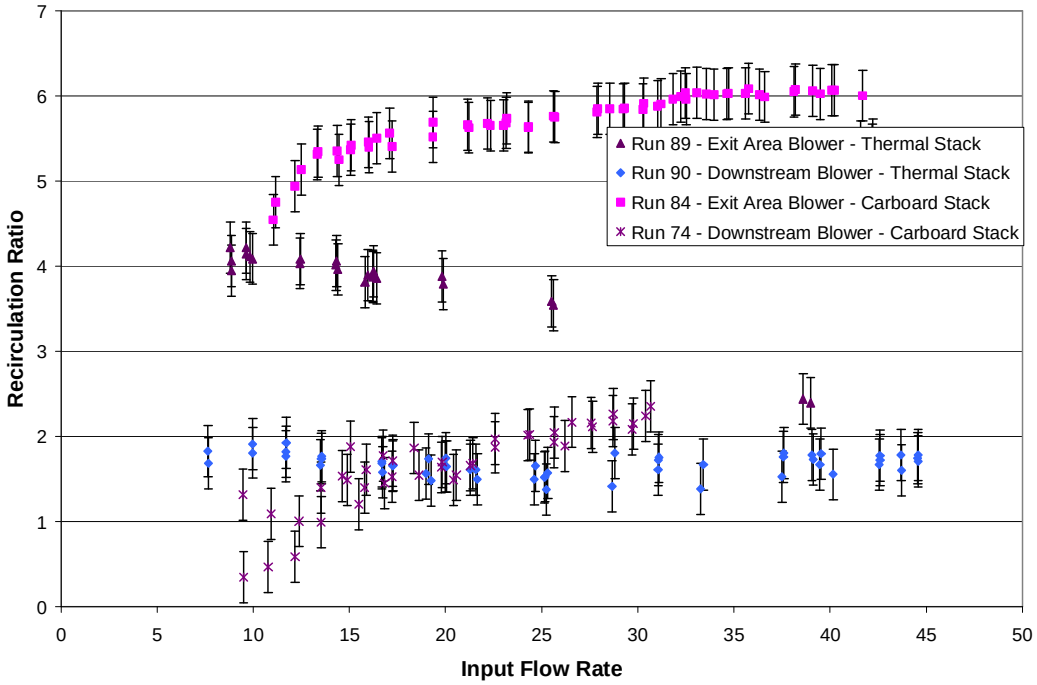

Figure 3.3.1 – Fluid mechanics comparison between thermal stack replica and initial cardboard stack replica (U_R=±0.30)

Using the exit area blower, tests were conducted on the effect of different stack temperatures on the metric T*. The data taken at the various temperatures from 110 ^{o}F to 140 ^{o}F are displayed graphically in Figure 3.3.4. When investigating the figure, it is evident that at the higher recirculation ratios there is an upper limit in the thermal mixing ratio. This can be attributed to heat losses in the experimental setup. At higher flow rates in the tunnel, more heat will be lost through the plexi-glass walls, sheet metal plenums, and through the wood base. These convective and conductive heat losses are more prevalent at both higher mass flow rates (higher recirculation ratios) and at higher temperatures (higher T* and stack temperatures). This maximum of approximately 0.6 for T^* could be a result of competing effects. The positive trend of an increase of thermal

mixing due to an increase of recirculation ratio is competing with a reduction of thermal mixing ratio due to heat losses inherent in the experimental setup. It seems as though the heat losses dominate at higher recirculation ratios, seen in Figures 3.3.2, 3.3.3, and 3.3.4.

From Figure 3.3.4, it appears there is an incremental effect of the stack temperature on the thermal mixing ratio. A recommendation for future work is to determine the effects of increasing the stack temperature both in the current test rig and a test rig that can sustain higher temperatures with lower heat losses (e.g. more insulated). The ultimate goal when implementing this system is to operate at temperatures near 1472 ^{o}F (800^{o}C). The results of Figure 3.3.4 show that the thermal mixing may be scalable to within the temperatures tested. Although, the heat losses of the experimental setup limit the quantification of the scaling of the results. Further higher temperature testing with monitored or lower heat losses may be able to prove that the system can scale to SOFC operating temperatures.

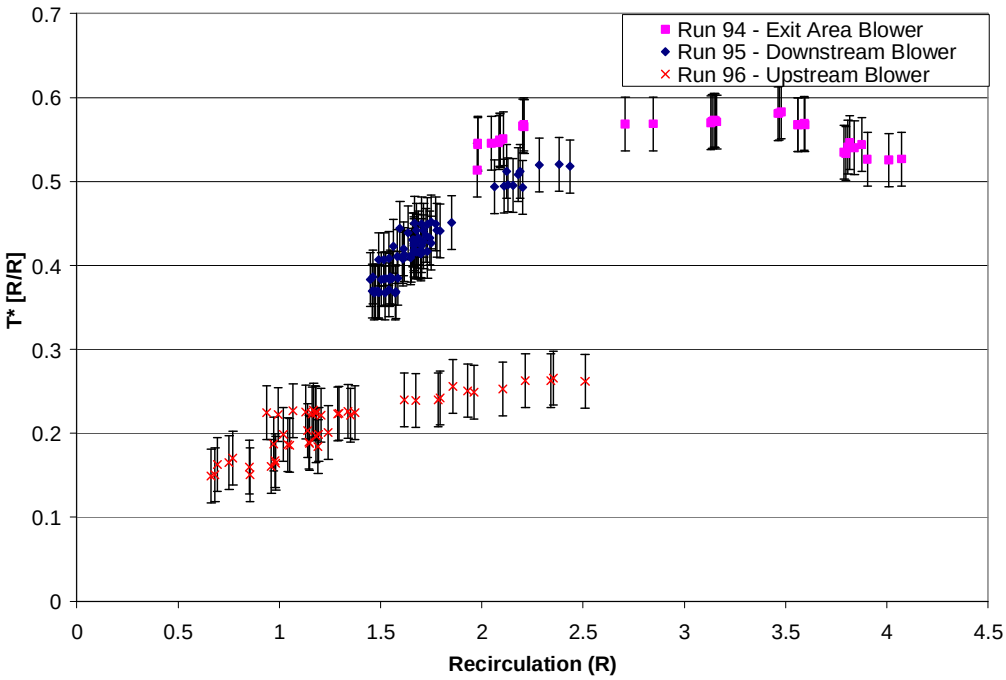

Figure 3.3.2 – Thermal mixing capabilities comparison of each blower at 140^{o}F (U_{T^*}=±0.032) (U_{R^*}=±0.30)

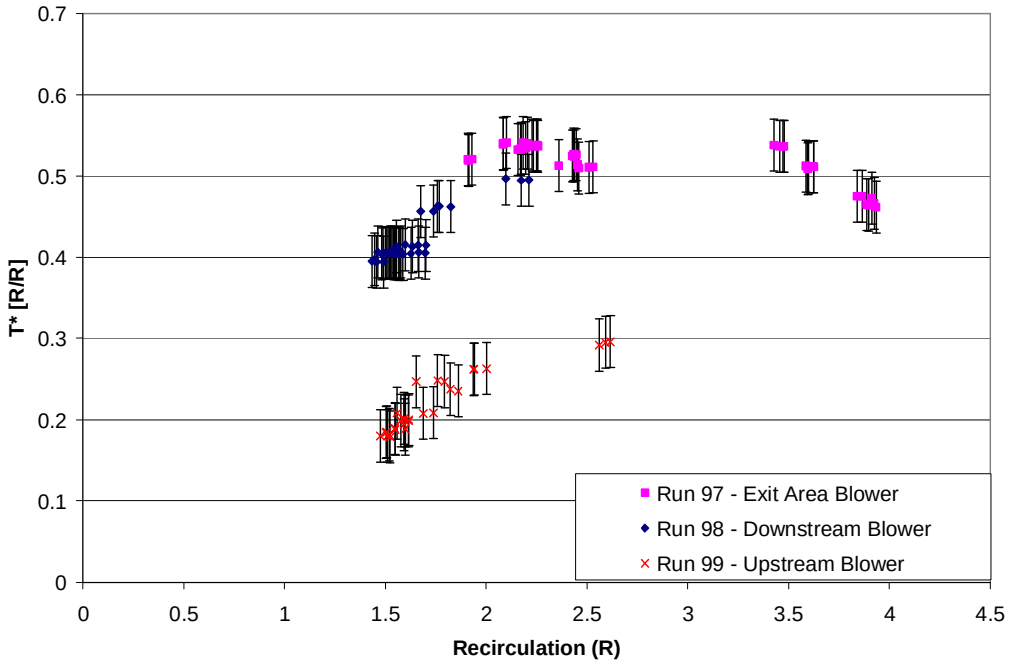

Figure 3.3.3 – Thermal mixing capabilities comparison of each blower at 160°F (U_{T*}=±0.032) (U_{R*}=±0.30)

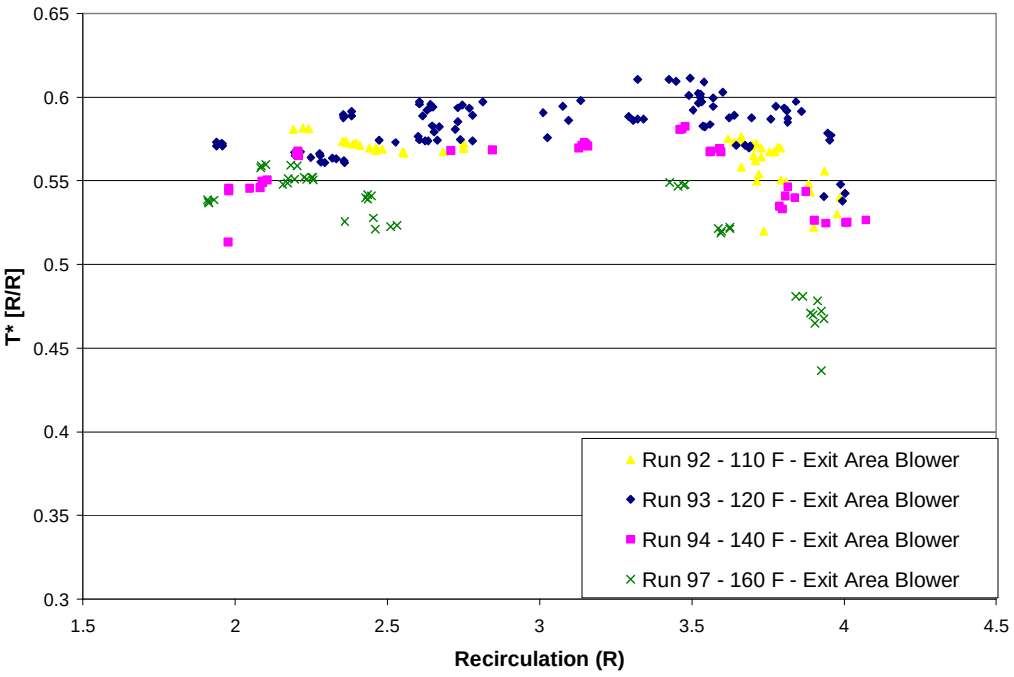

Figure 3.3.4 – Thermal mixing comparison of the test setup at different stack temperatures (110-160 °F) (U_{T*}=±0.032) (U_{R*}=±0.30)

3.4 – Discussion of Experimental Results

The goal of this phase of the project was to investigate if the multiple supply point entrainment approach was feasible. This chapter has discussed the results obtained from the experimental setup used to mimic the cathodic air supply thermal management. The fluid mechanic testing conducted using the cardboard stack replica has shown that the Coanda effect can be utilized to create entrained recirculation. Reducing the return path cross-sectional area with the foam insert allowed for a perceived reduction in vortices and/or backflow effects, and in turn an increase in the recirculation ratio. It was determined that the exit area blower was most effective in producing this recirculation. The exit area blower creates a "pneumatic door" that controls the air purged from the system allowing greater recirculation ratios. The experimental results have shown that recirculation is possible with multiple blowers.

The thermal results show that thermal mixing is possible with all of the blowers. However, the exit area blower was most effective in thermally mixing the air, for the domain tested. Providing higher recirculation allows for less heat to be purged from the system, thereby increasing the thermal mixing ratio. With the downstream and upstream blowers, it appeared that thermal mixing increased with an increase in recirculation ratio. Confirming the EES analysis discussed in Chapter 4, the thermal seed results demonstrated thermal mixing is more substantial when the incoming air is introduced downstream of the stack prior to the purge. The thermal mixing ratio seemed to have a maximum with respect to the temperatures tested and was most evident at the higher temperatures and the higher recirculation ratios. The thermal seed results presented help to conclude that this approach can provide pre-heating to the air leaving the blower. With enough preheating *in-situ*, the cathodic air pre-heater can be greatly reduced in cost and size.

CHAPTER 4

THERMODYNAMIC ANALYSIS OF THERMAL MANAGEMENT

To determine the thermodynamic feasibility of this approach a thermodynamic analysis was conducted on the overall system. This idealized model was developed to evaluate variable cases for thermal mixing within the multiple supply point entrainment approach. The equation set used for the Engineering Equation Solver (EES) analysis is included in Appendix C. The analysis is based specifically on the thermodynamic laws and mass conservation. EES is primarily used for a thermal systems analysis and the model discussed does not characterize the viscous losses associated with the thermal management approach. The following simulation will further prove the thermodynamic feasibility of this system as well as provide a useful tool in modeling the effects of altering different thermal parameters of the system.

4.1 – Schematic of the System Model and Assumptions

The system was modeled as 12 different thermal fluid states. The schematic for the modeled system is included in Figure 4.1.1. Each state is defined in Table 4.1.1. The adiabatic pressure drops are useful in quantifying the exergy of heat in the heat exchanger. The heat exchanger was included to make the model more robust; however, during initial modeling this heat exchanger was bypassed for simplicity.

A few assumptions were made when developing the model. The upstream and downstream control volumes are modeled as adiabatic processes with complete thermal mixing. It is assumed that the air leaving the fuel cell stack is at the stack temperature. A heat input into the air stream is the by-product heat generation (5 kW for a 5 kW stack) at the stack location. The stack rig in this model is ideally presumed to be adiabatic in regards to envelope losses. The NOS or “number of stoich’s” is determined from the mass of air necessary to maintain the stack at constant temperature.

The stack is assumed to have by-product heat equal to that of the power output. The compressor is assumed to be 90 % efficient at all operating conditions. The results discussed are for a 5kW stack power generator.

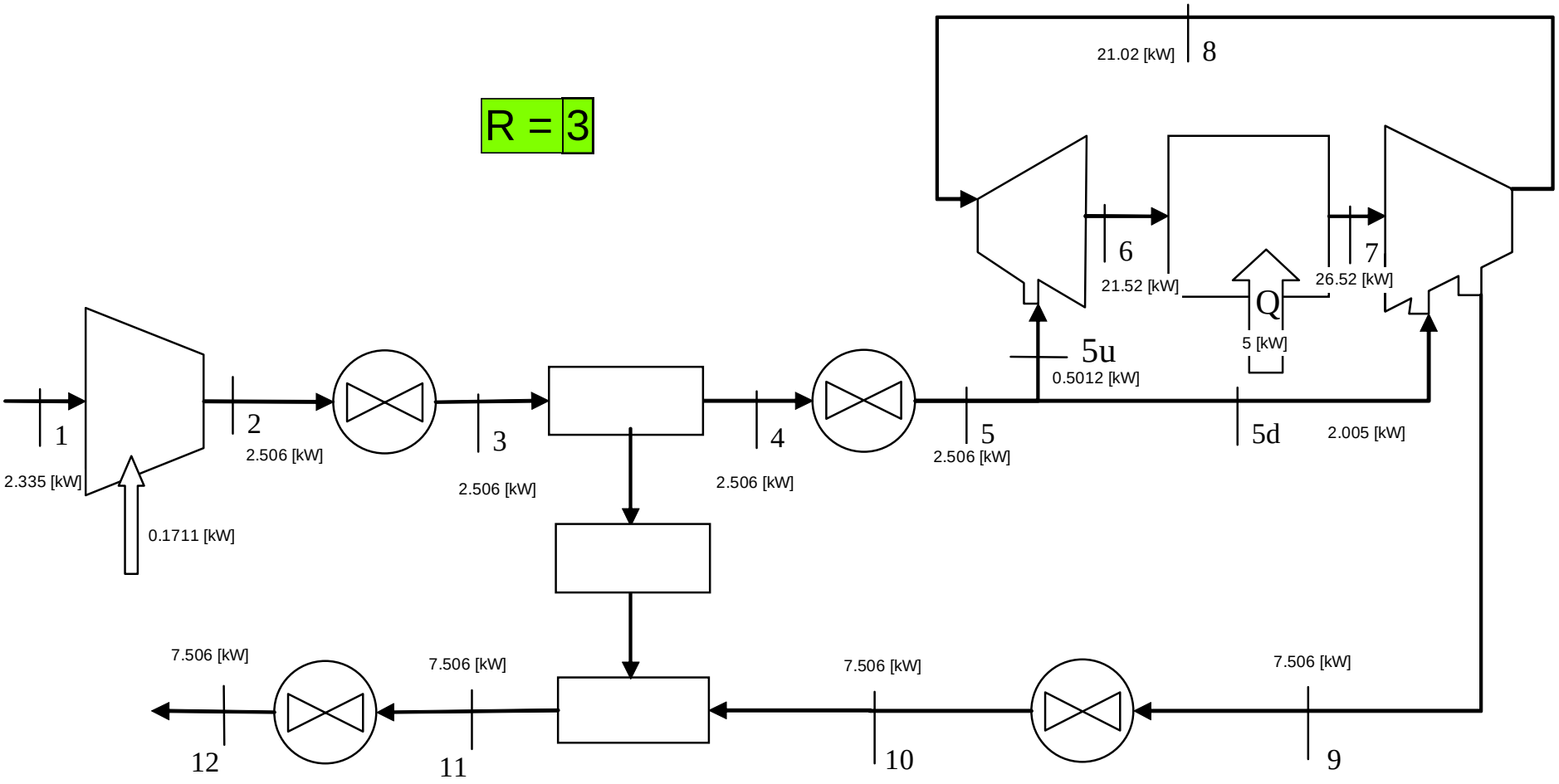

Figure 4.1.1 – SOFC recirculation model used for investigation of the thermodynamic feasibility. Includes the extensive energy at each of the 12 states (5 kW fuel cell stack)

Table 4.1.1 – Description of each of the states and processes in the SOFC recirculation model

SOFC Modeling States and Processes	
State	**State Description**
1	Ambient air prior to compression
2	Post compression air at a higher pressure
3	After adiabatic pressure drop prior to the cold side of the heat exchanger
4	Prior to adiabatic pressure drop post heat exchanger
5	Post adiabatic pressure drop, prior to split between the blowers
5u	Upstream blower air entering the adiabatic control volume upstream of the stack
5d	Downstream blower air entering the adiabatic control volume downstream of the stack
6	After upstream control volume entering the stack
7	After the heat input from the stack
8	After the downstream control volume, entering the upstream control volume
9	Purge exiting the downstream control volume, entering the adiabatic pressure drop on the hot side of the heat exchanger
10	After the adiabatic pressure drop, entering the hot side of the heat exchanger
11	Exiting the hot side of the heat exchanger, entering the adiabatic pressure drop
12	Exiting the adiabatic pressure drop and expelling to the atmosphere
Process	**Process Description**
1 → 2	Compressor raises the air pressure
2 → 3	Adiabatic pressure drop
3 → 4	Cold side of the gas to gas heat exchanger
4 → 5	Adiabatic pressure drop
5 → 5u,5d	Mass flow splits between the two plenums
5u,8 → 6	Upstream adiabatic control volume, Assumes complete thermal mixing
5d,7 → 8,9	Downstream adiabatic control volume, Assumes complete thermal mixing
6 → 7	Heat input from electrochemical reaction
9 → 10	Adiabatic pressure drop
10 → 11	Hot side of the gas to gas heat exchanger
11 → 12	Adiabatic pressure drop

4.2 – Important Equations Applying Continuity and the First Law

The model was based on application of the mass continuity equation and the First Law of thermodynamics. For the continuity equation, the sum of the mass flow(s) entering any control volume is equal to the sum of the mass flow(s) exiting the control volume. Equation 4.2.1 explains this application symbolically:

$$\sum_{in} \dot{m}_i = \sum_{out} \dot{m}_j \tag{4.2.1}$$

where $\sum_{in} \dot{m}_i$ is the sum of the mass flow(s) entering the control volume and $\sum_{out} \dot{m}_j$ is the sum of the mass flow(s) out of the control volume.[4] This application was critical in determining the mass flows into and out of the upstream and downstream adiabatic control volumes. The energy equation was applicable for each process in the modeled system. The applicable form of the 1st Law of Thermodynamics or the energy equation is for a steady-flow system, presented in equation 4.2.2:

$$\dot{Q}_{in} + \dot{W}_{in} + \sum_{in} \dot{m}_i h_i = \dot{Q}_{out} + \dot{W}_{out} + \sum_{out} \dot{m}_j h_j \tag{4.2.2}$$

where $\dot{Q}_{in}$ is input heat, $\dot{Q}_{out}$ is the output heat, $\dot{W}_{in}$ is the power input, $\dot{W}_{out}$ is the power output, and h is the enthalpy of the air. The First Law is applied to each steady flow device. Potential energy and kinetic energy were neglected due to their trivial contribution to the energy equation. The principles discussed were then applied to get the implications discussed in the next section

4.3 – EES Model Results and Implications

The developed EES model was able to describe the thermal mixing capabilities of the MSP approach. The model also can illustrate how different parameters (e.g. recirculation ratio, NOS, stack temperature, etc.) can affect the thermal properties throughout the system. With minor modifications other metrics can be investigated.

---

[4] Note that small decreases in cathodic airflow due to oxygen consumption are not considered in the present, preliminary analysis. The percentage reduction on mass is anticipated to be small.

In order to investigate the ideal thermal mixing capabilities of the system the thermal mixing ratio, T^*, was evaluated with differing recirculation ratios. A plot of this result is displayed in Figure 4.3.1. The plot of the thermal mixing ratio illustrates that the pre-heater can be excluded and even eliminated at presently feasible recirculation ratios (e.g., above 3.7). It is important to note that these results are independent of power rating and are scalable to different stack power ratings. When multiple power ratings were tested using the model, the equivalent "R vs. T^*" figure was produced. The thermal mixing ratio for a 250 kW fuel cell stack is approximately 0.8. This assumes a 43^{o}C air temperature leaving the blower, stack temperature of 800^{o}C, and an inlet air temperature required at 650^{o}C [TIAX, 2002]. Chapter 5 contains another preliminary First Law modeling result that confirms the exclusion of the air pre-heater at modest recirculation ratios.

During experimentation, recirculation ratios as high as 6 and thermal mixing ratios above 0.6 were seen. This implies that this approach may be able to significantly reduce the need for a bulky high temperature gas to gas heat exchanger, if higher thermal mixing ratios can be obtained. A new test setup with lower heat losses may prove to get higher thermal mixing ratios. In order for full thermal mixing to occur, a longer mixing channel than the one presented in the experimental setup may be required. Alternatively, the purge air will be at a lower temperature in the downstream case, and this will result in less thermal energy being advectively withdrawn. Instead more thermal energy can be recuperated. This is an idealized adiabatic model and performance results are expected to be below those shown here.

It is also important to note the split between the blowers has an effect on the thermal mixing ratio of the system. In Figure 4.3.2, the percent of mass flow through the downstream blower is compared to the thermal mixing ratio. As seen in the thermal testing, blowing from the downstream blower causes more effective thermal mixing in the recirculation system. Primarily supplying the air from the downstream blower allows the incoming air to thermally mix with a higher temperature and higher mass flow stream (air exiting the stack) than that of the air injected upstream of the stack (air entering the upstream control volume). The air exiting the stack includes the air that will be purged from the system. The air entering the upstream control volume does not include this air

that has been purged from the system. This means there is more localized heat transfer capacity and a larger rise in incoming air enthalpy when the downstream approach is taken. This result was also confirmed with the thermal seed test results presented in Chapter 3.

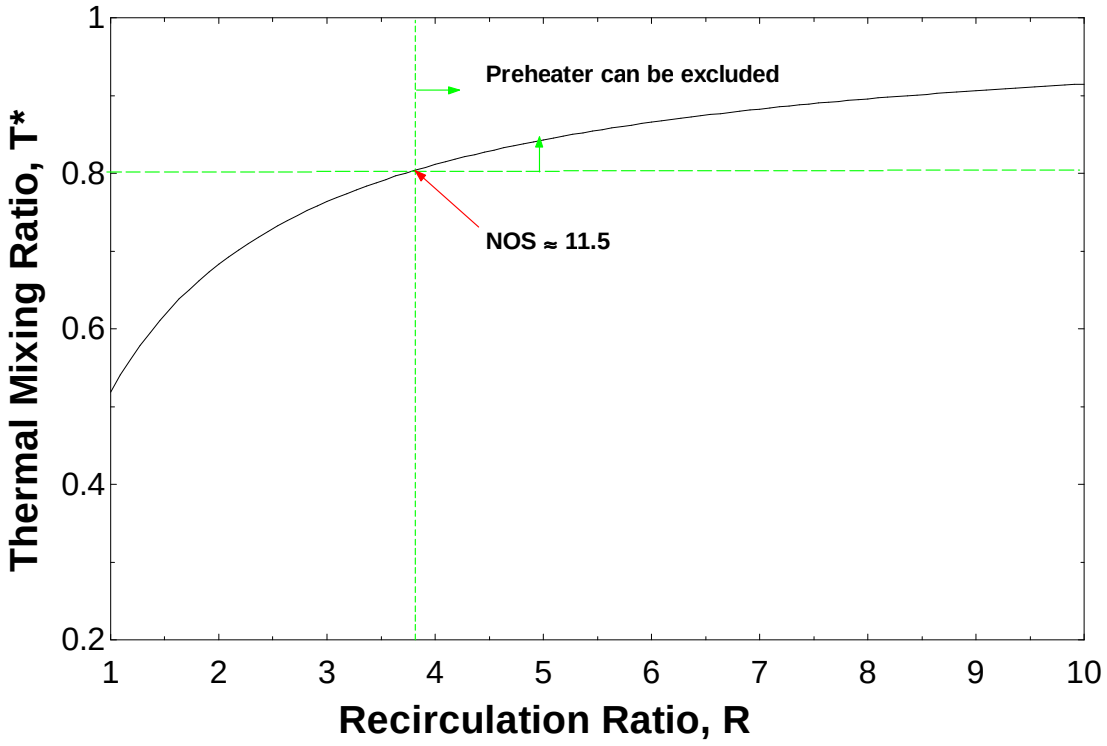

Figure 4.3.1 – EES plot showing the thermal mixing ratio vs. the recirculation ratio for a stack temperature of 700 ^{o}C

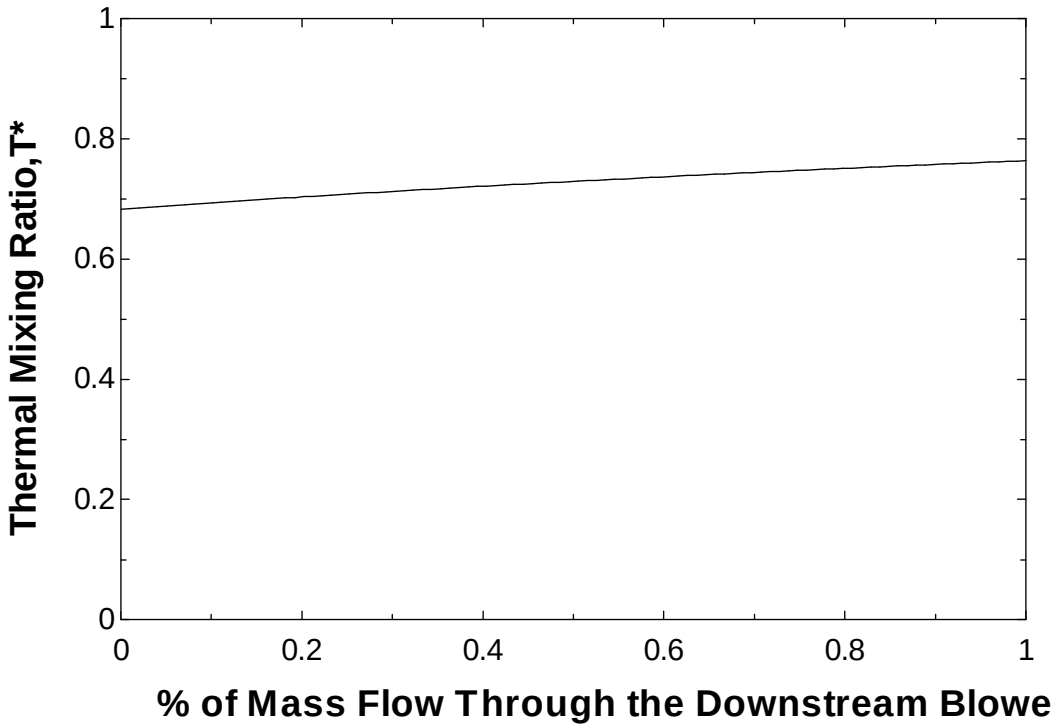

Figure 4.3.2 – EES plot illustrating the thermal mixing ratio vs. the percent mass flow through the downstream blower for a stack temperature of 700 ^{o}C, and R=3.

When conducting an exergy analysis, the benefits of using the MSP recirculation system are evident. Figure 4.3.3 shows the flow exergy and exergy destruction throughout the modeled system. The calculations for the exergy are included in Appendix C with the rest of the EES equations. It is evident that the air stream is able to enter the system at low exergy (states 1-5) and is still able to provide the stack with the necessary heated air by recovering some of the exergy of the air leaving the stack.

4.4 – Recommendations on Model Improvements

In order to further quantify the benefits over the large gas-to-gas heat exchanger cathodic preheat, a comparable model should be developed for a system with a heat exchanger without recirculation. Also, the model of the recirculation should be modified to include a smaller gas-to-gas heat exchanger, since preheating may still be required even with the proposed approach. The model is limited in characterizing the fluid mechanics of the thermal management approach. Specifically, the inclusion of viscous

losses and the momentum equation would improve the fidelity of the model. The overall model is useful in determining how different parameters affect the thermodynamics of the system.

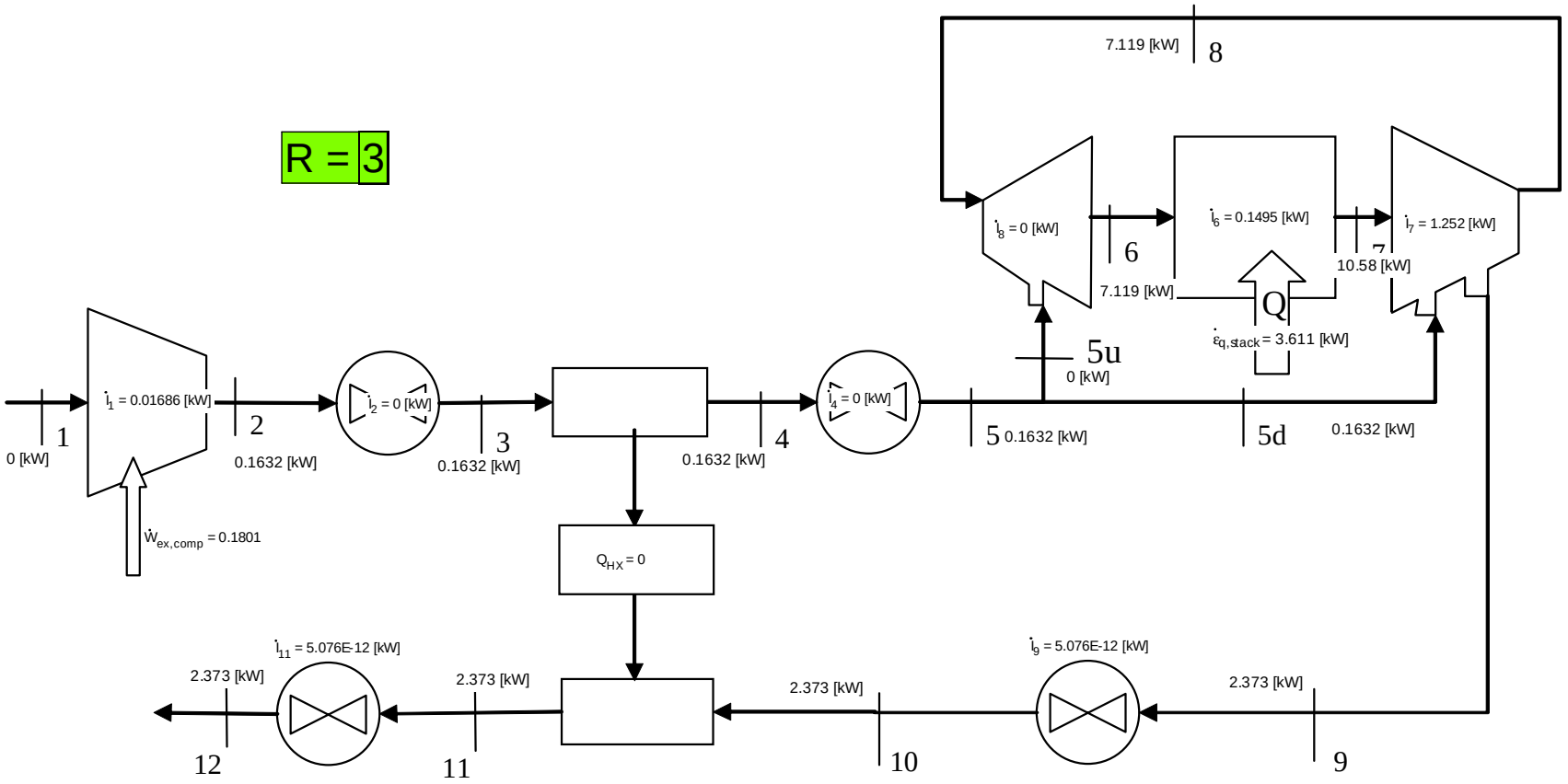

Figure 4.3.3 – SOFC recirculation model used for investigation of the thermodynamic feasibility. Includes the flow exergy and exergy destruction, $\dot{I}$, at each of the 12 states (5 kW fuel cell stack)

CHAPTER 5

PERFORMANCE AND ECONOMIC INCENTIVES

The purpose of the innovation discussed in this paper is to reduce the cost, weight, volume, and simultaneously increase the energy efficiency, of the high temperature fuel cell system. The following chapter introduces the improvements that this new system could make to a high temperature fuel cell system. With the proposed approach, the exclusion of the high temperature gas to gas heat exchanger is possible with modest recirculation, as well as a reduction in blower size and blower parasitic power loss. This chapter includes a discussion of the cost reductions this thermal management approach has over the conventional SOFC system.

5.1 – Cost Breakdown of a SOFC system

The components that this innovation attempts to minimize are the blower (rotating equipment) and the air preheat (recuperator). Figure 5.1.1 displays the typical cost breakdown for a 250 kW SOFC system. The "Rotating Equipment" and the "Recuperators" nominally make up 29% of the total cost of the SOFC system [TIAX, 2002]. If the cathode side blower and recuperator parasitics can be reduced then the cost of the system can greatly decline. Tables 5.1.1 and 5.1.2 show the relative cost, weight, and size of different recuperators in a SOFC system. The cathode air preheat is by far the largest and most expensive preheater. The enormous size of the cathode air preheat is attributable to the low heat transfer coefficient associated with air to air heat exchange. The low heat transfer coefficient necessitates a large surface area for effective heat transfer. Not only will the minimization or exclusion of the cathode air preheat benefit the system economically but also on a size and parasitics (i.e., attendant head loss) basis.

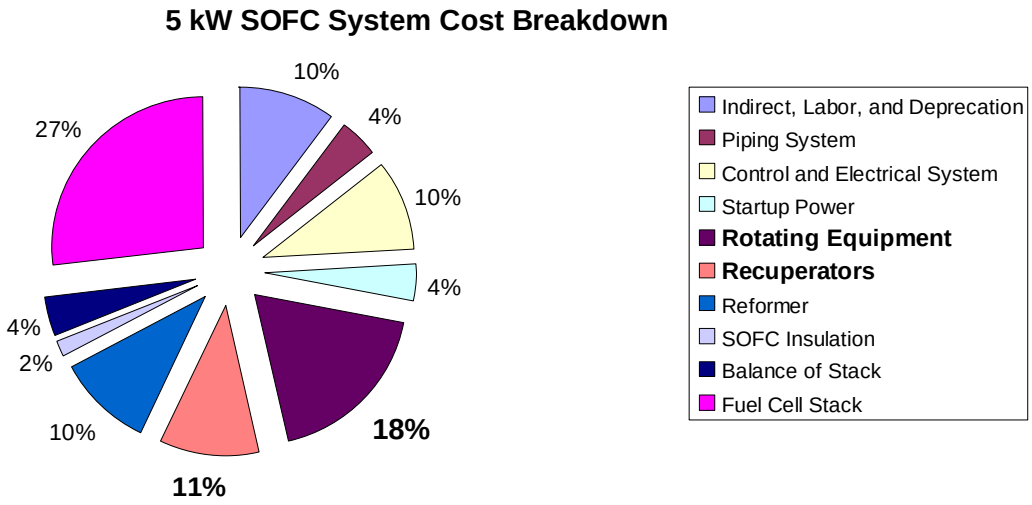

Figure 5.1.1 – Cost breakdown of a 5 kW SOFC system [TIAX, 2002]

Table 5.1.1 – Comparison of the different recuperators in a 250 kW SOFC system using a plate and fin design [TIAX, 2002]

Superheated Steam Generator	Dimensions (in)	18.65 x 14.06 x 1.5
	Weight (lbs)	25.4
Fuel Preheat	Dimensions (in)	5.35 x 5.62 x 1.5
	Weight (lbs)	Included in Steam Generator
Fuel and Steam Preheat One	Dimensions (in)	6.0 x 6.2 x 6.0
	Weight (lbs)	11
Cathode Air Preheat	Dimensions (in)	40.53 x 55 x 50
	Weight (lbs)	6,178

Source: Stewart Warner South Wind

Table 5.1.2 – Relative cost comparison of the different recuperators in a 250 kW SOFC system using a shell and tube design – Bos Hatten [TIAX, 2002]

Superheated Steam Generator	Length (ft)	5.10
	Diameter (ft)	0.38
	Cost ($)	8,281
Steam Generator	Length (ft)	8.90
	Diameter (ft)	2.00
	Cost ($)	17,222
Fuel Preheat	Length (ft)	6.70
	Diameter (ft)	0.55
	Cost ($)	10,815
Fuel and Steam Preheat One	Length (ft)	7.00
	Diameter (ft)	0.72
	Cost ($)	12,927
Fuel and Steam Preheat Two	Length (ft)	8.70
	Diameter (ft)	0.72
	Cost ($)	18,934
Cathode Air Preheat	Length (ft)	23.10
	Diameter (ft)	2.17
	Cost ($)	144,948

NOTES:
1. Shell and tube designs; 1 unit per year production
Source Bos-Hatten

Table 5.1.1 and 5.1.2 show two different quotes for the different heat exchangers in a SOFC system. Table 5.1.1 displays the cathode air preheat in a 250 kW system at a size of 40.53 x 55 x 50 inches and a weight of over 6000 pounds. This data was quoted directly from Stewart Warner South Wind, a heat exchanger manufacturer. The preceding discussion demonstrates that the cathode air preheat is a large portion of an SOFC system on a mass, spatial, and cost basis. If it can be reduced or eliminated the cost, mass, and volume of an SOFC system can be greatly reduced. Both testing and modeling have shown that the cathode air preheat can be reduced or even excluded.

5.2 – Preheat Reduction

A solid oxide fuel cell system is more than just the fuel cell stack. Numerous components work together to make the system perform effectively and efficiently. An overall schematic of a candidate fuel cell system is re-displayed in Figure 5.2.1. The air preheater is a bulky, high temperature gas to gas heat exchanger. This bulky heat exchanger also has large pressure losses associated with it. As shown in the previous section, if the air preheat can be eliminated or even reduced in size, the cost of the overall system will be reduced.

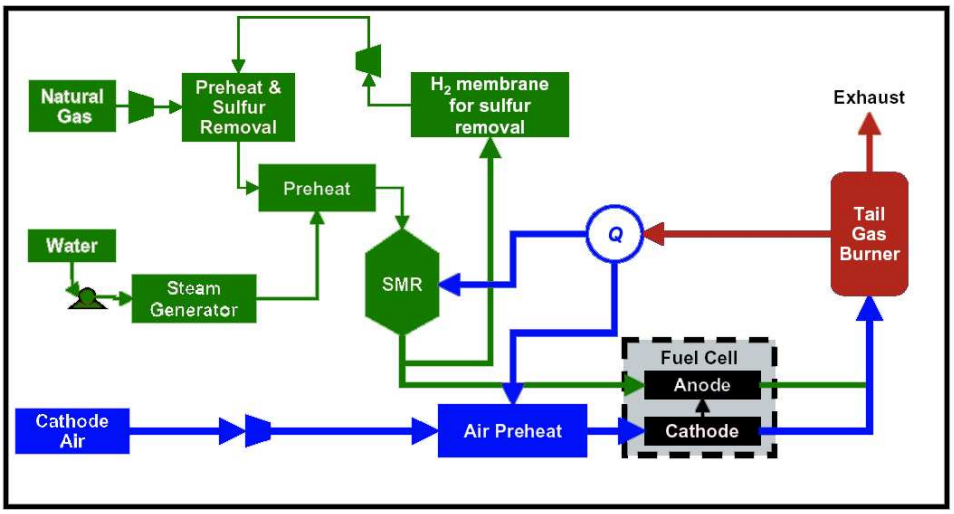

Figure 5.2.1 – Schematic showing some of the components that make up a solid oxide fuel cell system [Agnew, 2004]

With the proposed design, on a purely thermal analysis basis, the air preheat can be eliminated with modest recirculation. Figure 5.2.2 was developed making the following assumptions/simplifications:

Large NTU within cathodic flow channels, $\therefore T_{air,DS} \approx T_{stack} = 750^{o} C$

$C_p \approx const \approx C_p(T_{stack})$

$$\dot{m}_{air,circulated} = \frac{I_{equivalent} \cdot NOS_{supplied} \cdot \beta \cdot M_{air} \cdot (\#O_2 / H_2)}{n \cdot F}$$

Based on a 5 kW stack, 50 % efficiency

$I_{equivalent} = 7143A$, based on $V_{cell} = 0.7$ V

$q_{rxn} = 5000W$

where C_p is the specific heat, $T_{air,DS}$ is the temperature of the air leaving the stack, T_{stack} is the temperature of the stack, $\dot{m}_{air,circulated}$ is the mass of air flowing through the stack, $I_{equivalent}$ is the equivalent (stoichiometric) current from the stack, $NOS_{supplied}$ is the required "number-of-stoichs" for the stack (i.e., actual-to-theoretical oxidant supply), β is the moles of air per mole of O_2, M_{air} is the molar mass of air, n is the number of electrons per mol of O_2, F is Faraday's constant, $\#O_2 / H_2$ is the moles of O_2 per mole of H_2, V_{cell} is the cell voltage, and q_{rxn} is the heat release from the reactions.

The NOS=11.5 confirms the results discussed in the EES model in Chapter 4. The major difference in the two analyses is that the EES analysis requires the air going through the stack to be able to sufficiently maintain the stack at a constant temperature. The NOS is variable depending on the heat of reaction (5 kW). The analysis here allows the NOS to be set. With the recirculation ratios that are observed from experimentation, the air preheat can be eliminated. Qualitatively similar cathodic air recirculation developments in Europe espouse this possibility [Agnew, 2004]. Although the air preheat may be greatly reduced or eliminated, this approach will also require extensive insulation to reduce the heat losses of the tunnel. The high air temperatures inside the setup will require significant insulation, increasing the system cost. To further develop the cost comparison, an initial analysis on the cost of the advanced thermal management concept needs to be performed.

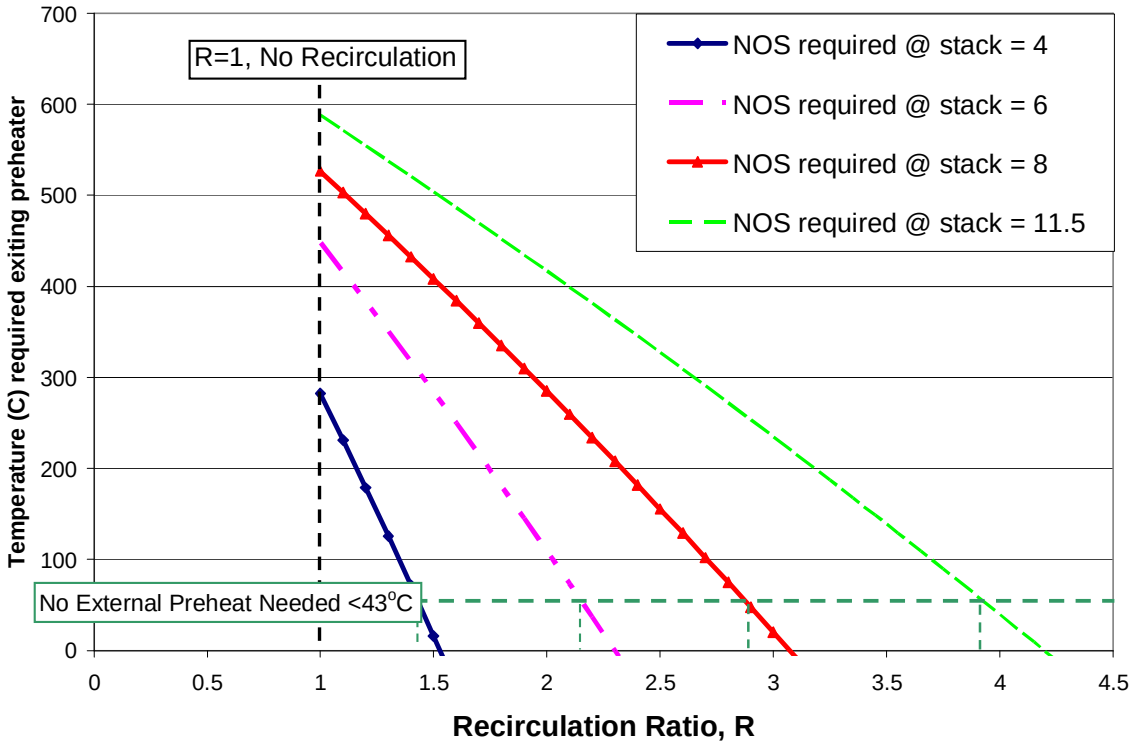

Figure 5.2.2 – Thermal analysis illustrates that the air preheat can be eliminated with obtainable recirculation ratios; this initial analysis has a First Law basis. (Note: NOS=11.5 matches the preheater exclusion point in the EES analysis discussed in Chapter 4.)

5.3 – Blower or Compressor Reduction

The blower size may be reduced by re-circulating the air in the system. A preliminary analysis on the blower supply reduction was conducted in Figure 5.3.1. There is a significant reduction in the necessary NOS (number-of-stoichs) supplied. The analysis for this figure was done by using the simple equation 5.3.1.

$$NOS_{\text{sup }plied} = \frac{NOS_{required}}{R} \qquad (5.3.1)$$

Where $NOS_{supplied}$ is amount of air supplied from the blower and $NOS_{required}$ is the amount of air required by the stack. With a reduction in blower supply rate, there is a potential reduction in blower parasitics (cost, weight, and spatial size). The additional head

requirement for recirculation, however, may be a significant counter-effect. Further investigation of the balance between lower mass flow requirements and higher pressure ratio would reveal the requirements for the blower in this approach.

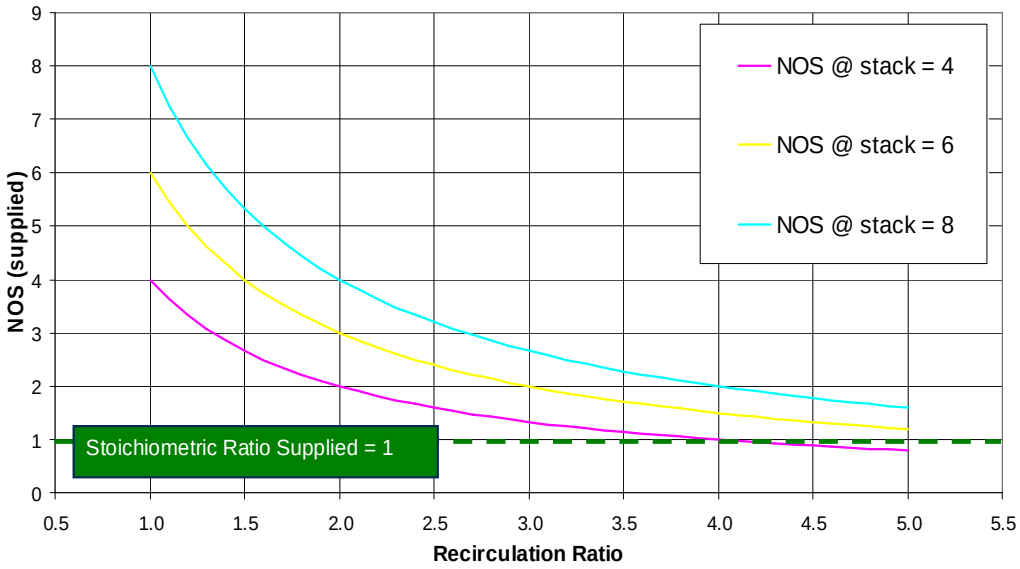

Figure 5.3.1 – Preliminary analysis of blower supply reduction

CHAPTER 6

CONCLUSIONS AND RECOMMENDATIONS FOR FUTURE WORK

Testing has shown that the Coandă effect can be utilized to circulate the flow inside this system. Positive recirculation ratios have been achieved using the Coandă blowers. It seems that having multiple blowers activated has declining effects from a fluid dynamics standpoint. It is hypothesized that the opposing vectors in the experimental setup have a counter-acting effect. Progressive improvements in the key metric of recirculation ratio were empirically realized through modifying test rig cross-sectional area and activating alternative blowing slots (e.g., the exit area blowing slot).

From the thermal perspective it appears as though thermal mixing is more significant if applied downstream of the SOFC stack. The incoming air mixes with the higher temperature and higher mass flow air stream exiting the stack, as opposed to the lower temperature lower mass flow air stream entering the upstream control volume. This concept is confirmed both experimentally and through the EES model. It was noticed that increasing the recirculation ratio increased the thermal mixing ratio and therefore the air temperature. This increased both the thermal mixing and the thermal heat losses. A maximum thermal mixing ratio was noticed in the experimental setup and was attributed to a balance between increased thermal mixing and increased thermal losses intrinsic to the setup. The exit area blower, operating like a “pneumatic door”, seemed to be the most effective from both the fluid dynamic and thermal mixing perspective. More experimental investigation into the thermal properties of the fluid flow with multiple blowers is needed to see the overall effect of multiple supply points. The use of upstream blowers still may be effective for guiding the flow into the stack

channels. With use of the Coandă effect and multiple supply points less viscous losses are expected within the system, compared to ejectors.

When investigating the system on the basis of First and Second Laws of Thermodynamics, it is evident that thermal mixing in the system is possible. From the EES analysis, the complete elimination of the high temperature gas to gas heat exchanger may be possible. The results of the EES analysis show that the reduction of the cathodic air preheat is a definite possibility with the active flow control system, confirming the results from the thermal seed testing. With the reduction of the cathode air preheat and cathode blower, significant reductions can be made in the cost, size, and weight of the SOFC system.

Future work can concentrate on improving the fluid mechanics and thermal mixing characteristics using computational fluid dynamics (CFD). After the CFD code is developed (including verification), it should be utilized to redesign a test setup for higher fidelity thermal and fluid mechanic testing. Another recommendation for future work is to determine the effects of increasing the stack temperature in a redesigned test rig that can sustain higher temperatures with lower heat losses. After the further testing, a preliminary design may be developed to compare directly to conventional cathode SOFC designs as well as the ejector approach. With a preliminary design, an expanded cost, weight, and size estimate for the proposed system will strengthen the argument of the potential economic and viability benefits of this approach.

APPENDIX A

REQUIRED MASS FLOW RATE CALCULATIONS

The following calculations were used to determine the mass flow rate of air through the stack that is necessary for the desired Number of Stoichs (NOS). The calculations presented are based on a 5 kW stack with a power density typical of a SOFC.

$$\mathrm{p_{typical}} = \text{Typical Power Density} = 0.5\ \mathrm{W/cm^2}$$ [EG&G, 2004]

Each cell has an active area, A_A, (electrochemical reaction area) of 400 $\mathrm{cm^2}$.

$$\mathrm{A_A} = \text{Active Area} = 400\ \mathrm{cm^2}\ /\ Cell$$

The stack consists of 25 cells, N_{cells}.

$$N_{cells} = 25$$

$$P_{stack} = N_{cells} A_A p_{typical} = (0.5\ \mathrm{W/cm^2})(400\ \mathrm{cm^2}\ /\ Cell)(25\ \text{cells}) = 5{,}000\ \mathrm{W}$$

The following assumptions were made to complete the calculations:

$$\mathrm{V_{cell}} = \text{Cell Voltage} = 0.7\ \mathrm{V}$$

$$\mathrm{I_{effective}} = \text{Current x number of cells} = \mathrm{P_{stack}}\ /\ V_{cell} = 7143A$$

β is the ratio of the moles of air for each mole of diatomic oxygen in atmospheric air. M_{air} is the molar mass of air. ν_{O_2} is the ratio of diatomic oxygen to diatomic hydrogen in the stoichiometric electrochemical reaction. n is the number of electrons for each diatomic oxygen. F is faraday's constant.

$$\beta = 4.76\ \mathrm{mol\,air\ /\ mol\,O_2}$$

$$M_{Air} = 28.97 \text{ g air / mol air}$$

$$\nu_{O_2} = 0.5 \text{ mol } O_2 \text{ / mol } H_2$$

$$nF = 193{,}000 \text{ C/mol } H_2$$

The equation for mass flow becomes:

$$\dot{m}_{air} = \frac{I_{effective} \cdot \nu_{O_2}}{nF} NOS \cdot \beta \cdot M_{Air}$$

where $I_{effective}$ is the effective stoichiometric current required for the power output and NOS is the "number of stoichs". For the air required going through the stack in the recirculation system it follows that:

$$\dot{m}_{air,required} = \frac{7143\, C/s * 0.5 \text{ mol } O_2 \text{ / mol } H_2}{193{,}000 \text{ C/mol } H_2} (NOS_{required})(4.76 \text{ mol air / mol } O_2)(28.97 \text{ g air / mol air})$$

$$\dot{m}_{air,required} = 2.55 g \text{ /s} * \text{NOS}_{\text{required}}$$

$$\dot{m}_{air,required} = \frac{.0025518\, kg}{s} * \frac{2.205 lb_m}{kg} * \frac{783.9 SCFM}{lb_m / s} = 4.411 \text{SCFM} * \text{NOS}_{\text{required}}$$

The air required to supply through the blowers, $\dot{m}_{air,\text{supplied}}$ is therefore:

$$\Rightarrow \dot{m}_{air,\text{supplied}} = \frac{4.411 \text{ SCFM} * NOS_{required \text{ at stack}}}{\text{Re} \, circulation \, Ratio}$$

APPENDIX B

RECIRCULATION RATIO UNCERTAINTY QUANTIFICATION

The following analysis discusses the calculation of the recirculation ratio inside the test rig and conducts a comprehensive measurement uncertainty analysis based on error propagation. Recirculation Ratio is calculated from equation A-1:

$$\mathrm{R} = \frac{\dot{m}_{circulated}}{\dot{m}_{\mathrm{sup}\ plied}} \tag{A-1}$$

where $\dot{m}_{circulated}$ (equation A-2) is the mass circulating through the stack replica and $\dot{m}_{\mathrm{sup}\ plied}$ (equation A-3) is the mass supplied to the tunnel via the plenums, calculated from the critical flow nozzles (CFNs).

$$\dot{m}_{circulated} = \rho \cdot v \cdot A = \left(\frac{P_{stat}}{R_{air} T_{amb}}\right)\left(\sqrt{\frac{2(P_{tot,avg} - \mathrm{P}_{\mathrm{stat}})}{\rho}}\right)(A)$$

$$\dot{m}_{circulated} = \left(\frac{P_{stat}}{R_{air} T_{amb}}\right)\left(\sqrt{2R_{air} T_{amb}\left(\frac{P_{tot,avg}}{P_{stat}} - 1\right)}\right)(A) \tag{A-2}$$

$$\dot{m}_{\mathrm{sup}\ plied} = \frac{c_1 P_{inlet}^{\ 3} + c_2 P_{inlet}^{\ 2} + c_3 P_{inlet}}{60\sqrt{T_{amb}}} \tag{A-3}$$

where $\mathrm{P}_{\mathrm{stat}}$ is the static pressure downstream of the stack, $\mathrm{P}_{\mathrm{tot,avg}}$ is the average total pressure downstream of the stack, ρ is the density, v is the bulk velocity through the stack, $\mathrm{T}_{\mathrm{amb}}$ is the ambient temperature in the tunnel, $\mathrm{R}_{\mathrm{air}}$ is the gas constant for air, A is the area, $\mathrm{P}_{\mathrm{inlet}}$ is the static pressure at the inlet to the CFN, and c_1, c_2, c_3 are calibration constants of the Flow-Dyne CFNs. The uncertainty of $\dot{m}_{\mathrm{sup}\ plied}$ is taken from Flow-Dyne website as 0.66 SCFM [Flow-dyne, 2006]. The overall equation of the recirculation ratio becomes equation A-4:

$$\mathrm{R} = \frac{1}{\dot{m}_{\sup plied}}\left(\frac{P_{stat}}{R_{air}T_{amb}}\right)\left(\sqrt{2R_{air}T_{amb}\left(\frac{P_{tot,avg}}{P_{stat}} - 1\right)}\right)(A) \qquad \text{(A-4)}$$

Using the propagation of uncertainties, the uncertainty in the recirculation ratio is calculated using equation A-5:

$$U_R{}^2 = \left(\left(\partial R / \partial P_{stat}\right)\left(U_{P_{stat}}\right)\right)^2 + \left(\left(\partial R / \partial P_{tot,avg}\right)\left(U_{P_{tot,avg}}\right)\right)^2 + \left(\left(\partial R / \partial T_{amb}\right)\left(U_{T_{amb}}\right)\right)^2$$
$$+ \left(\left(\partial R / \partial \dot{m}_{\sup plied}\right)\left(U_{\dot{m}_{\sup plied}}\right)\right)^2 + \left(\left(\partial R / \partial A\right)\left(U_A\right)\right)^2 \qquad \text{(A-5)}$$

The calculations following are based on one specific data point with only the exit area plenum blowing.

$$T_{amb} = 530.84°\mathrm{R}$$
$$\mathrm{A} = 0.1778\,ft^2$$
$$P_{stat} = 14.4371 psia$$
$$P_{tot,avg} = 14.4411 psia$$
$$\dot{m}_{\sup plied} = 2.111 \bullet 10^{-3}\, lb/s$$

The calculation of the uncertainties in each measurement is the root sum of the squares of the elemental errors, i.e.:

$$U_{P_{stat}} = \sqrt{U_{resolution}{}^2 + U_{accuracy}{}^2 + U_{calibration}{}^2}$$
$$U_{P_{stat}} = U_{P_{tot,avg}} = \sqrt{(6.1 \bullet 10^{-5}\, psid)^2 + (.0002 * 1 psid)^2 + (.001 psid)^2} = 0.1471 psfd$$

$$U_{T_{amb}} = \sqrt{U_{resolution}{}^2 + U_{accuracy}{}^2} = \sqrt{(0.25°C)^2 + (0.1°C)^2} = 0.2692°C * 1.8\,\Delta°F/\Delta°C = 0.4847°F$$

The above elemental uncertainties were extracted from the Pressure Systems 8400 manual and Tempscan temperature scanner manual. The area uncertainty is based on the uncertainty of the amount of blockage through the stack replica. The mass supplied uncertainty is taken from Flow Dyne's specifications for the CFN.

$$U_A = 2\%(0.0933) = 0.001867\, ft^2 \leftarrow \text{Aluminum Thermal Stack}$$
$$U_A = 10\%(0.1776) = 0.01776\, ft^2 \leftarrow \text{Cardboard Stack}$$
$$U_{\dot{m}_{supplied}} = 8.33 \bullet 10^{-4}\, lb/s = 0.66 SCFM$$

The partial derivatives with respect to each independent measurement are calculated:

$$\partial R / \partial \dot{m}_{supplied} = -\frac{A}{\dot{m}_{supplied}^{\ 2}} \left(\frac{P_{stat}}{R_{air} T_{amb}}\right)\left(\sqrt{2 R_{air} T_{amb}\left(\frac{P_{tot,avg}}{P_{stat}} - 1\right)}\right)$$

$$\partial R / \partial A = \frac{1}{\dot{m}_{supplied}} \left(\frac{P_{stat}}{R_{air} T_{amb}}\right)\left(\sqrt{2 R_{air} T_{amb}\left(\frac{P_{tot,avg}}{P_{stat}} - 1\right)}\right)$$

$$\partial R / \partial P_{stat} = \frac{A}{\dot{m}_{supplied}} \left[\begin{array}{l} \left(\frac{1}{R_{air} T_{amb}}\right)\left(\sqrt{2 R_{air} T_{amb}\left(\frac{P_{tot,avg}}{P_{stat}} - 1\right)}\right) \\ + \left(\frac{P_{stat}}{2 R_{air} T_{amb}}\right)\left(-2 R_{air} T_{amb} \frac{P_{tot,avg}}{P_{stat}^{\ 2}}\right)\left(2 R_{air} T_{amb}\left(\frac{P_{tot,avg}}{P_{stat}} - 1\right)\right)^{-1/2} \end{array} \right]$$

$$\partial R / \partial P_{stat} = \frac{A}{\dot{m}_{supplied}} \left[\left(\frac{1}{R_{air} T_{amb}}\right)\left(\sqrt{2 R_{air} T_{amb}\left(\frac{P_{tot,avg}}{P_{stat}} - 1\right)}\right) + \left(-\frac{P_{tot,avg}}{P_{stat}}\right)\left(2 R_{air} T_{amb}\left(\frac{P_{tot,avg}}{P_{stat}} - 1\right)\right)^{-1/2} \right]$$

$$\partial R / \partial P_{tot,avg} = \frac{A}{\dot{m}_{supplied}} \left(\frac{P_{stat}}{R_{air} T_{amb}}\right)\left(\frac{R_{air} T_{amb}}{P_{stat}}\right)\left(2 R_{air} T_{amb}\left(\frac{P_{tot,avg}}{P_{stat}} - 1\right)\right)^{-1/2} = \frac{A}{\dot{m}_{supplied}}\left(2 R_{air} T_{amb}\left(\frac{P_{tot,avg}}{P_{stat}} - 1\right)\right)^{-1/2}$$

$$\partial R / \partial T_{amb} = \frac{A}{\dot{m}_{supplied}} \left[\begin{array}{l} -\left(\frac{P_{stat}}{R_{air} T_{amb}^{\ 2}}\right)\left(2 R_{air} T_{amb}\left(\frac{P_{tot,avg}}{P_{stat}} - 1\right)\right)^{1/2} \\ + \left(\frac{P_{stat}}{R_{air} T_{amb}}\right)\left(R_{air}\left(\frac{P_{tot,avg}}{P_{stat}} - 1\right)\right)\left(2 R_{air} T_{amb}\left(\frac{P_{tot,avg}}{P_{stat}} - 1\right)\right)^{-1/2} \end{array} \right]$$

Using the propagation of uncertainties presented in equation A-5, the overall measurement uncertainty in R is 0.4 for the thermal stack and 0.9 for the cardboard stack.

At a recirculation ratio of 5.5, the % uncertainty is 7.3% for the thermal stack and 16 % for the cardboard stack. This is the uncertainty of one data point. After Run79, the recorded data points are an average of 100 successive points, which greatly reduces the uncertainty. Taking a 100 point average provides sufficient accuracy for determining trends in the test rig. The data recorded before the data averaging (Run 79 and before) has more uncertainty associated with it; however, some of the trends discovered were useful for determining areas of future testing.

APPENDIX C

EES EQUATION SET FOR MODELING THE SOFC APPROACH

C.1 EES Solutions

An example solution of the EES simulation with a recirculation ratio of 3 is presented in this section. Tables C.1.1 shows the most important results and Table C.1.2 shows the rest of the results.

Table C.1.1 – Solution to EES simulation of the recirculation approach

T[i]	h[i]	H_ext[i]	s[i]	S_ext[i]	Ex_dot[i]	ex[i]
[C]	[kJ/kg]	[kW]	[kJ/kg-K]	[kW/K]	[kW]	[kW/kg]
25	298.6		5.699			0
25	298.6	2.458	5.699	0.04692	0	0
46.76	320.4	2.638	5.706	0.04697	0.1632	19.83
46.76	320.4	2.638	5.706	0.04697	0.1632	19.83
46.76	320.4	2.638	5.706	0.04697	0.1632	19.83
46.76	320.4	2.638	5.706	0.04697	0.1632	19.83
622	927.8	22.91	6.843	0.169	7.119	288.3
800	1130	27.91	7.052	0.1742	10.58	428.4
622	927.8	22.91	6.843	0.169	7.119	288.3
622	927.8	7.638	6.843	0.05633	2.373	288.3
622	927.8	7.638	6.843	0.05633	2.373	288.3
622	927.8	7.638	6.843	0.05633	2.373	288.3
622	927.8	7.638	6.843	0.05633	2.373	288.3

Table C.1.2 – Other solutions to EES simulation of the recirculation approach

Beta=4.76 [mol·air·/·mol·O2]	P[0]=100 [kPa]
deltaP_HX=0 [kPa]	P[1]=100 [kPa]
deltaP_stack=1 [kPa]	P[2]=125 [kPa]
Epsilon_dot_q_stack=3.611 [kW]	P[3]=125 [kPa]
Eta_comp=0.9	P[4]=125 [kPa]
Ex_dot_5d=0.1632 [kW]	P[5]=125 [kPa]
Ex_dot_5u=0 [kW]	P[6]=101 [kPa]
HX_effectiveness=0.9	P[7]=100 [kPa]
H_ext_5d=2.638 [kW]	P[8]=101 [kPa]
H_ext_5u=0 [kW]	P[9]=101 [kPa]
h_s[2]=318.3 [kJ/kg]	P[10]=101 [kPa]
I_effective=7143	P[11]=101 [kPa]
M_air=28.97 [g·air/mole·air]	P[12]=101 [kPa]
m_dot_d=0.008232 [kg/s]	P_r=1.25
m_dot_exit=0.008232 [kg/s]	P_tunnel=101 [kPa]
m_dot_input=0.008232 [kg/s]	Q=5 [kW]
m_dot_stack=0.0247 [kg/s]	Q_HX=0
m_dot_tunnel=0.0247 [kg/s]	Q_stack=5 [kW]
m_dot_u=0 [kg/s]	R=3
m_R=1	T_stack=800 [C]
nF=193000 [C/mol·H2]	T_star=0.7637
NOS=9.679	V_cell=0.7 [V]
Nu_O_2=0.5	w_comp_s=19.69 [kJ/kg]
Power_Stack=5 [kW]	W_dot_ex_comp=0.1801
w_comp=21.88 [kJ/kg]	

C.2 EES Equation Set

The following displays the Equation set used for the solution set presented in Table C.1.1, Table C.1.2, and in Chapter 4:

Operating conditions

$T_{stack} = 800$ [C]

R = 3 Recirculation Ratio

Assuming 50% efficiency

$Q_{stack} = Power_{Stack}$

Percent mass flow through the downstream blower

$m_R = 0.8$

Pressure ratio and efficiency in the compressor

$P_r = 1.25$

$\eta_{comp} = 0.9$

Heat exchanger effectiveness

$HX_{effectiveness} = 0.9$

Stack mass flow calculations

$M_{air} = 28.97$ [g·air/mole·air]

$V_{cell} = 0.7$ [V]

$Power_{Stack} = 5$ [kW]

$$I_{effective} = Power_{Stack} \cdot \frac{1000}{V_{cell}}$$

$nF = 193000$ [C/mol·H2]

$\beta = 4.76$ [mol·air·/·mol·O2]

$\nu_{O,2} = 0.5$

$$\dot{m}_{stack} = \nu_{O,2} \cdot \frac{I_{effective}}{nF} \cdot \beta \cdot M_{air} \cdot \frac{NOS}{1000}$$

$$R = \frac{\dot{m}_{stack}}{\dot{m}_{input}}$$

Dimensionless Temperature

$$T_{star} = \frac{T_6 - T_3}{T_{stack} - T_3}$$

Ambient Conditions

$P_0 = 100$ [kPa]

$T_0 = 25$ [C]

$h_0 = \mathbf{h}('Air', T = T_0)$

$s_0 = \mathbf{s}('Air', T = T_0, P = P_0)$

Restricted dead state / Used for exergy calculations

$$ex_0 = h_0 - (T_0 + 273.15) \cdot s_0 - (h_0 - (T_0 + 273.15) \cdot s_0)$$

State 1: Prior to compression – ambient air

$P_1 = P_0$

$T_1 = T_0$

$h_1 = h_0$

$s_1 = s_0$

State 2: Post compression – Prior to heat exchanger

$P_2 = P_1 \cdot P_r$

$$h_{s,2} = \mathbf{h}('Air', P = P_2, s = s_1)$$

$$w_{comp,s} = h_{s,2} - h_1$$

$$w_{comp} = \frac{w_{comp,s}}{\eta_{comp}}$$

$$w_{comp} = h_2 - h_1$$

$$\dot{W}_{ex,comp} = w_{comp} \cdot \dot{m}_{input}$$

$$T_2 = \mathbf{T}('Air', h = h_2)$$

$$s_2 = \mathbf{s}('Air', h = h_2, P = P_2)$$

State 3: After Adiabatic pressure drop - Prior to the cold side of the heat exchanger"
Heat exchanger bypassed for simplicity

$$\delta P_{HX} = 0 \quad [kPa]$$

$$P_3 = P_2 - \frac{\delta P_{HX}}{2}$$

$$h_3 = h_2$$

$$T_3 = \mathbf{T}('Air', h = h_3)$$

$$s_3 = \mathbf{s}('Air', h = h_3, P = P_3)$$

State 4: After the cold side of the heat exchanger – Before the adiabatic pressure drop"
Heat exchanger bypassed for simplicity

$$h_4 = h_3$$

$$T_4 = \mathbf{T}('Air', h = h_4)$$

$$P_4 = P_3$$

$$s_4 = \mathbf{s}('Air', h = h_4, P = P_4)$$

$$P_5 = P_4 - \frac{\delta P_{HX}}{2}$$

State 5: After the the adiabatic pressure drop – Prior to splitting of streams"
Heat exchanger bypassed for simplicity

$$h_5 = h_4$$

$$T_5 = \mathbf{T}('Air', h = h_5)$$

$$s_5 = \mathbf{s}('Air', h = h_5, P = P_5)$$

Mass balance inside the recirculation CVs

State 5d: Downstream mass flow

$$\dot{m}_d = \dot{m}_{input} \cdot m_R$$

State 5u: Upstream mass flow

$$\dot{m}_u = \dot{m}_{input} \cdot (1 - m_R)$$

Upstream CV mass balance

$$\dot{m}_u + \dot{m}_{tunnel} = \dot{m}_{stack}$$

Downstream CV mass balance

$$\dot{m}_d + \dot{m}_{stack} = \dot{m}_{tunnel} + \dot{m}_{exit}$$

State 6: After upstream control volume

$$P_{tunnel} = 101 \quad [kPa]$$

$$P_6 = P_{tunnel}$$

$$\dot{m}_u \cdot h_5 + \dot{m}_{tunnel} \cdot h_8 = \dot{m}_{stack} \cdot h_6$$

$$T_6 = \mathbf{T}('Air', h = h_6)$$

$$s_6 = \mathbf{s}('Air', h = h_6, P = P_6)$$

State 7: After the stack entering the downstream CV

$$\delta P_{stack} = 1$$

$$P_7 = P_6 - \delta P_{stack}$$

$$h_6 + \frac{Q}{\dot{m}_{stack}} = h_7$$

$$\dot{m}_{stack} \cdot h_7 + \dot{m}_d \cdot h_5 = \dot{m}_{tunnel} \cdot h_8 + \dot{m}_{exit} \cdot h_9$$

$$T_7 = T_{stack}$$

$$h_7 = \mathbf{h}('Air', T = T_7)$$

$$s_7 = \mathbf{s}('Air', h = h_7, P = P_7)$$

State 8: After the downstream CV – Entering the upstream CV

$$h_8 = h_9$$

$$T_8 = \mathbf{T}('Air', h = h_8)$$

$$P_8 = P_{tunnel}$$

$$s_8 = \mathbf{s}('Air', h = h_8, P = P_8)$$

State 9: Purge from downstream CV – towards adiabatic pressure drop on hot side of the HX
HX bypassed for simplicity

$$P_9 = P_8$$

$$T_9 = \mathbf{T}('Air', h = h_9)$$

$$s_9 = \mathbf{s}('Air', h = h_9, P = P_9)$$

State 10: After adiabatic pressure drop – towards hot side of the HX
HX bypassed for simplicity

$$P_{10} = P_9 - \frac{\delta P_{HX}}{2}$$

$$h_{10} = h_9$$

$$T_{10} = \mathbf{T}(\text{'Air'}, h = h_{10})$$

$$s_{10} = \mathbf{s}(\text{'Air'}, h = h_{10}, P = P_{10})$$

State 11: After hot side of HX – towards adiabatic pressure drop after hot side of the HX
HX bypassed for simplicity

$$P_{11} = P_{10}$$

$$T_{11} = T_{10}$$

$$h_{11} = \mathbf{h}(\text{'Air'}, T = T_{11})$$

$$s_{11} = \mathbf{s}(\text{'Air'}, h = h_{11}, P = P_{11})$$

State 12: After adiabatic pressure drop – Purge to the environment

$$P_{12} = P_{11} - \frac{\delta P_{HX}}{2}$$

$$h_{12} = h_{11}$$

$$T_{12} = \mathbf{T}(\text{'Air'}, h = h_{12})$$

$$s_{12} = \mathbf{s}(\text{'Air'}, h = h_{12}, P = P_{12})$$

Extensive Entropy

$$S_{ext,1} = s_1 \cdot \dot{m}_{input}$$

$$S_{ext,2} = s_2 \cdot \dot{m}_{input}$$

$$S_{ext,3} = s_3 \cdot \dot{m}_{input}$$

$$S_{ext,4} = s_4 \cdot \dot{m}_{input}$$

$$S_{ext,5} = s_5 \cdot \dot{m}_{input}$$

$$S_{ext,6} = s_6 \cdot \dot{m}_{stack}$$

$$S_{ext,7} = s_7 \cdot \dot{m}_{stack}$$

$$S_{ext,8} = s_8 \cdot \dot{m}_{tunnel}$$

$$S_{ext,9} = s_9 \cdot \dot{m}_{exit}$$

$$S_{ext,10} = s_{10} \cdot \dot{m}_{exit}$$

$$S_{ext,11} = s_{11} \cdot \dot{m}_{exit}$$

$$S_{ext,12} = s_{12} \cdot \dot{m}_{exit}$$

Extensive Enthalpy

$$H_{ext,1} = h_1 \cdot \dot{m}_{input}$$

$$H_{ext,2} = h_2 \cdot \dot{m}_{input}$$

$$H_{ext,3} = h_3 \cdot \dot{m}_{input}$$

$$H_{ext,4} = h_4 \cdot \dot{m}_{input}$$

$$H_{ext,5} = h_5 \cdot \dot{m}_{input}$$

$$H_{ext,6} = h_6 \cdot \dot{m}_{stack}$$

$$H_{ext,7} = h_7 \cdot \dot{m}_{stack}$$

$$H_{ext,8} = h_8 \cdot \dot{m}_{tunnel}$$

$$H_{ext,9} = h_9 \cdot \dot{m}_{exit}$$

$$H_{ext,10} = h_{10} \cdot \dot{m}_{exit}$$

$$H_{ext,11} = h_{11} \cdot \dot{m}_{exit}$$

$$H_{ext,12} = h_{12} \cdot \dot{m}_{exit}$$

$$H_{ext,5u} = H_{ext,5} \cdot (1 - m_R)$$

$$H_{ext,5d} = H_{ext,5} \cdot m_R$$

Determination of heat input into the air moving into the stack

$$Q = \textbf{If}(Q, Q_{stack}, H_{ext,7} - H_{ext,6}, 5, 5)$$

Flow Exergy

$$ex_1 = h_1 - (T_0 + 273.15) \cdot s_1 - (h_0 - (T_0 + 273.15) \cdot s_0)$$

$$ex_2 = h_2 - (T_0 + 273.15) \cdot s_2 - (h_0 - (T_0 + 273.15) \cdot s_0)$$

$$ex_3 = h_3 - (T_0 + 273.15) \cdot s_3 - (h_0 - (T_0 + 273.15) \cdot s_0)$$

$$ex_4 = h_4 - (T_0 + 273.15) \cdot s_4 - (h_0 - (T_0 + 273.15) \cdot s_0)$$

$$ex_5 = h_5 - (T_0 + 273.15) \cdot s_5 - (h_0 - (T_0 + 273.15) \cdot s_0)$$

$$ex_6 = h_6 - (T_0 + 273.15) \cdot s_6 - (h_0 - (T_0 + 273.15) \cdot s_0)$$

$$ex_7 = h_7 - (T_0 + 273.15) \cdot s_7 - (h_0 - (T_0 + 273.15) \cdot s_0)$$

$$ex_8 = h_8 - (T_0 + 273.15) \cdot s_8 - (h_0 - (T_0 + 273.15) \cdot s_0)$$

$$ex_9 = h_9 - (T_0 + 273.15) \cdot s_9 - (h_0 - (T_0 + 273.15) \cdot s_0)$$

$$ex_{10} = h_{10} - (T_0 + 273.15) \cdot s_{10} - (h_0 - (T_0 + 273.15) \cdot s_0)$$

$$ex_{11} = h_{11} - (T_0 + 273.15) \cdot s_{11} - (h_0 - (T_0 + 273.15) \cdot s_0)$$

$$ex_{12} = h_{12} - (T_0 + 273.15) \cdot s_{12} - (h_0 - (T_0 + 273.15) \cdot s_0)$$

Extensive Flow Exergy

$$\dot{E}x_1 = ex_1 \cdot \dot{m}_{input}$$
$$\dot{E}x_2 = ex_2 \cdot \dot{m}_{input}$$
$$\dot{E}x_3 = ex_3 \cdot \dot{m}_{input}$$
$$\dot{E}x_4 = ex_4 \cdot \dot{m}_{input}$$
$$\dot{E}x_5 = ex_5 \cdot \dot{m}_{input}$$
$$\dot{E}x_6 = ex_6 \cdot \dot{m}_{stack}$$
$$\dot{E}x_7 = ex_7 \cdot \dot{m}_{stack}$$
$$\dot{E}x_8 = ex_8 \cdot \dot{m}_{tunnel}$$
$$\dot{E}x_9 = ex_9 \cdot \dot{m}_{exit}$$
$$\dot{E}x_{10} = ex_{10} \cdot \dot{m}_{exit}$$
$$\dot{E}x_{11} = ex_{11} \cdot \dot{m}_{exit}$$
$$\dot{E}x_{12} = ex_{12} \cdot \dot{m}_{exit}$$
$$\dot{E}x_{5u} = \dot{E}x_5 \cdot (1 - m_R)$$
$$\dot{E}x_{5d} = \dot{E}x_5 \cdot m_R$$

Heat exchanged

$$Q_{HX} = H_{ext,4} - H_{ext,3}$$

Exergy of Heat

$$\dot{\varepsilon}_{q,stack} = -\left[\frac{T_0 + 273.15}{T_{stack} + 273.15} - 1\right] \cdot Q$$

Exergy Destruction

$$\dot{I}_1 = \dot{E}x_1 + \dot{W}_{ex,comp} - \dot{E}x_1$$
$$\dot{I}_2 = -\dot{E}x_3 + \dot{E}x_2$$
$$\dot{I}_4 = -\dot{E}x_5 + \dot{E}x_4$$
$$\dot{I}_6 = -\dot{E}x_7 + \dot{E}x_6 + Q$$
$$\dot{I}_7 = -\dot{E}x_8 - \dot{E}x_9 + \dot{E}x_5 \cdot m_R + \dot{E}x_7$$
$$\dot{I}_8 = -\dot{E}x_6 + \dot{E}x_5 \cdot (1 - m_R) + \dot{E}x_8$$
$$\dot{I}_9 = -\dot{E}x_{10} + \dot{E}x_9$$
$$\dot{I}_{11} = -\dot{E}x_{12} + \dot{E}x_{11}$$

REFERENCES

Agnew, Gerry, "Novel Components for Reduced Costs", *ICEPAG-2004*, Irvine, 2004.

Agnew, G. D., Bozzolo, M., Moritz, R. R., and Berenyi, S., 2005, "The Design and Integration of the Rolls-Royce Fuel Cell Systems 1 MW SOFC," ASME Paper No. 2005-GT-69122, 2005.

Ameri, Mohammad, *An Experimental and Theoretical Study of Coanda Ejectors,* (Ann Arbor, MI: Case Western Reserve University, August 1993).

Camtecs, *http://camtecs.typepad.com/camtecs/images/stack250w_v6.jpg*. M ay, 2006.

Chemical Rubber Company (CRC). 1984. CRC Handbook of Chemistry and Physics. Weast, Robert C., editor. 65th edition. CRC Press, Inc. Boca Raton, Florida. USA.

EG&G Services, *Fuel Cell Handbook, Seventh Edition*, (Morgantown, WV: United States Department of Energy, 2004).

Figliola, Richard S., Beasley, Donald E., *Theory and Design for Mechanical Measurement*, 3rd Edition, New York: John Wiley and Sons, Inc., 2000.

Flow-dyne Engineering, Inc., "Critical Flow Nozzle, Bulletin 101", http://www.flow-dyne.com, September, 2006.

Hartvigsen, Joseph, "Ceramatec Flow Calculations", Internal Communication Email to Dr. Comas Haynes, Ceramatec, 2006.

Hay, I. F. C., Woolman, P. S., Wood, A., Higenbottam, T. W., "Accurate measurement of airway thermal challenge", *Clinical Physics and Physiological Measurement*, Great Britain, Vol. 9, No. 4, ppg. 331-337, 1988.

Jeter, Sheldon, "Implications of the Continuum Enthalpy Equation", *Fundamentals of Thermodynamics*, Georgia Institute of Technology, October 2005.

Larmine, J., and Dicks, Andrew, *Fuel Cell Systems Explained*, Chichester, England: Wiley & Sons, 2003.

Matweb, "Online Material Data Sheet: Overview - Acrylic, General Purpose, Molded" *http://www.matweb.com/search/SpecificMaterial.asp?bassnum=O1300*, February, 2007.

Maynes, D., Webb, B.W., "The effect of viscous dissipation in thermally fully-developed electro-osmotic heat transfer in microchannels", *International Journal of Heat and Mass Transfer.* Vol. 47, ppg. 987-999, 2004.

Munson, Bruce R., Young, Donald F., Okiishi, Theodore H., *Fundamentals of Fluid Mechanics*, 4th edition, New York: John Wiley and Sons, Inc., 2002.

Norwegian University of Science and Technology (NUST), *http://www.ept.ntnu.no/te/sofc_no.htm*, June, 2006.

Panitz, T. and Wasan, D.T., "Flow Attachment to Solid Surfaces: The Coanda Effect", *AlChE Journal*, Volume 18, Number 1, January 1972.

Pressure Systems, "System 8400 User's Manual", September, 2000.

Seimi Chemical, *http://www.seimichemical.co.jp/e/product/materials/ceramic.html*, 2001.

Steele, Brian and Heinzel, Angelika, "Materials for Fuel Cell Technologies", *Nature*, Volume 414, 2001.

TIAX, "Scale up Study of 5-kW SECA modules to a 250-kW system", June, 2002.

Transvac, "How do Ejectors Work?", *http://transvac.co.uk/*, June, 2006.

von Spakovsky, M.R.,"Technical Presentation". *PEMFC Senior Design Project*, Virginia Polytechnic Institute and State University, (August, 2004).